

# He abundance of Dense Circumstellar Clumps in the Cassiopeia A Supernova Remnant

BON-CHUL KOO,<sup>1,2</sup> DONGKOK KIM,<sup>1</sup> SUNG-CHUL YOON,<sup>1,2</sup> AND JOHN C. RAYMOND<sup>3</sup>

<sup>1</sup>*Department of Physics and Astronomy, Seoul National University, Seoul 08861, Republic of Korea*

<sup>2</sup>*Research Institute of Basic Sciences, Seoul National University, Seoul 08826, Republic of Korea*

<sup>3</sup>*Harvard-Smithsonian Center for Astrophysics, 60 Garden Street, Cambridge, MA 02138, USA*

## ABSTRACT

We report on the result of He abundance analysis of dense circumstellar clumps in the young supernova remnant Cassiopeia A. These clumps, which are called *quasi-stationary flocculi* (QSFs), are known from previous optical studies to be enriched in He along with N, but the degree of He overabundance relative to H has remained uncertain. For several QSFs with near-infrared spectroscopic data, we have analyzed their He I 1.083  $\mu\text{m}/\text{Pa}\gamma$  ratios together with the ratios of [Fe II] lines by using the Raymond shock code. According to our analysis, He is overabundant relative to H by a factor of  $\lesssim 3$  in most of these QSFs. This He abundance of QSFs is consistent with the previous conclusion from the N overabundance that QSFs were ejected when a substantial amount of the H envelope of the progenitor star had been stripped off. We discuss the mass-loss history of the progenitor star and the origin of QSFs.

**Keywords:** ISM — ISM : individual (Cassiopeia A) — supernovae : general — ISM: supernova remnants

## 1. INTRODUCTION

Young remnants of core-collapse supernovae (SNe) interact with circumstellar medium (CSM) ejected “immediately” before the explosion. By studying the physical and chemical characteristics of the CSM, we can learn how the progenitors stripped off their envelopes and exploded, which is crucial for understanding the nature of progenitors. In particular, the chemical abundance of the CSM is correlated with the proportion of the hydrogen envelope retained in the SN progenitor, which depends on various mass-loss processes from massive stars including radiation-driven winds, episodic mass eruptions, and/or binary interactions (e.g., Smith 2014; Yoon et al. 2017; Davies & Dessart 2019; Vink 2022), so that it can be used to infer the mass history of the SN progenitor star.

Cassiopeia A (Cas A) is one of the few supernova remnants (SNRs) where we can observe fine details of the mass-loss event. It is young ( $\sim 340$  yr; Thorstensen et al. 2001) and nearby (3.4 kpc; Reed et al. 1995; Alarie

et al. 2014). Its SN type is Type IIb, indicating that the progenitor had a thin H envelope at the time of explosion (Krause et al. 2008). The optical echo spectrum of the Cas A SN is very similar to that of SN 1993J, the progenitor of which was identified as a red supergiant (RSG) in early optical images (Aldering et al. 1994). The blast wave of the Cas A SNR is currently at  $\sim 2.5$  pc from the explosion center, and it is shown that the morphology and expansion rates are explained better by a model where the SNR is interacting with an RSG wind than by a model with a uniform ambient medium (Chevalier, & Oishi 2003). It is also found that the X-ray characteristics of the shocked ejecta knots and shocked ambient gas are consistent with Cas A expanding into an RSG wind of hydrogen density  $\sim 0.9 \text{ cm}^{-3}$  at the current outer radius of the remnant (Laming & Hwang 2003; Hwang & Laming 2009; Lee et al. 2014). However, the temporal evolution of the reverse shock suggests that the SN blast wave encountered a dense, asymmetrical circumstellar shell in the past (Orlando et al. 2022; Vink et al. 2022, see also Section 4.3). In the northern and eastern areas well outside the SNR, there are clumpy and filamentary H $\alpha$  nebulosities, some of which could be the remains of the progenitor’s RSG

wind (Minkowski 1968; van den Bergh 1971; Fesen et al. 1987; Chevalier, & Oishi 2003; Weil et al. 2020).

In addition to the diffuse CSM, there are distinct fine structures embedded in it. From the earliest optical studies, it has been known that there are almost “stationary” ( $\lesssim 400 \text{ km s}^{-1}$ ) nebulosities or knots bright in  $\text{H}\alpha$  and  $[\text{N II}] \lambda\lambda 6548, 6583$  emission line images (Peimbert & van den Bergh 1971; van den Bergh 1971; Kamper, & van den Bergh 1976; van den Bergh & Kamper 1983, 1985; Lawrence et al. 1995). Analysis of their optical spectra showed that these “quasi-stationary flocculi (QSFs)” are N-enriched, so that it is conjectured that they are CNO-processed circumstellar material ejected by the progenitor before SN explosion and have been shocked by the SN blast wave recently (Peimbert & van den Bergh 1971; McKee & Cowie 1975; Chevalier & Kirshner 1978; Alarie et al. 2014). There are about 40 QSFs identified from optical studies and they are scattered over the entire remnant (see also Koo et al. 2018). Some of them are aligned to form a prominent arc structure, indicating an eruptive mass-loss event. Chevalier & Kirshner (1978) carried out a detailed analysis of the optical spectra of two bright QSFs using a shock model and showed that N is overabundant relative to H by a factor of 7–10. Lamb (1978) showed that the observed high abundance of N matches that of the N-rich layer at the bottom of the H envelope of a 9–25  $M_{\odot}$  model star at the end of core H burning (see also Chevalier & Kirshner 1978). Chevalier & Kirshner (1978) also derived the He abundance for one of the two QSFs, but it had a large uncertainty due to extinction estimates, i.e., the derived He overabundance factor relative to H was 10 or 4 depending on whether the extinction ( $A_V$ ) was 4.3 or 6.5. The uncertain He abundance made the comparison with the stellar evolution models difficult (e.g., Lamb 1978).

In this paper, we explore the He abundance of QSFs using the He I 1.083  $\mu\text{m}$  emission line. The 1.083  $\mu\text{m}$  line is one of the strongest lines in nebular emission, and has been used to derive He abundance in Galactic HII regions and planetary nebulae as well as metal poor HII regions in external galaxies (Clegg 1987; Peimbert & Torres-Peimbert 1987; Clegg & Harrington 1989; Takami et al. 2002,b; Izotov et al. 2014; Aver et al. 2015). The intensity of the He I 1.083  $\mu\text{m}$  line, however, depends strongly on electron density, so that the line alone cannot provide an accurate He abundance. In shocked gas, we have an independent density indicator in the near-infrared (NIR) band, i.e.,  $[\text{Fe II}]$  lines (Dinerstein 1995; Nisini 2008; Koo et al. 2016).  $[\text{Fe II}]$  lines are strong in shocked gas because (1)  $\text{Fe}^+$  is the major ionization stage of Fe atoms, (2) the  $\text{Fe}^+$  ion

has many levels with low excitation energies that can be easily excited in shocked gas, and (3) Fe abundance can be enhanced by shocks owing to grain destruction (McKee, Chernoff, & Hollenbach 1984; Hollenbach & McKee 1989; Oliva, Moorwood, & Danziger 1989; Koo et al. 2016). (Note that  $[\text{Fe II}]$  lines are very faint in photoionized gas because Fe ions are mostly in higher ionization states and also presumably because Fe atoms fixed on dust grains.) Hence, from NIR spectroscopic observations on the ground, we can obtain a reliable estimate of both electron density and He abundance of shocked gas such as QSFs in Cas A.

We specifically use the He I 1.083  $\mu\text{m}/\text{Pa}\gamma$  ratio as the indicator of He abundance. The wavelengths of two lines are nearly the same (i.e., 1.083  $\mu\text{m}$  and 1.094  $\mu\text{m}$ ), so an extinction correction is not necessary. This is a great advantage for studying Cas A because the extinction to Cas A is large, e.g.,  $A_V \gtrsim 6$  (Hwang & Laming 2012; Lee et al. 2015; Koo & Park 2017, and references therein). For density diagnosis, we use the ratio of the sum of three  $[\text{Fe II}]$  lines at 1.534, 1.600, and 1.664  $\mu\text{m}$  to the  $[\text{Fe II}]$  1.644  $\mu\text{m}$  line. The former three  $[\text{Fe II}]$  lines are all density-sensitive lines with comparable critical densities, but much weaker than the 1.644  $\mu\text{m}$  line (e.g., see Koo et al. 2016). Note that the wavelengths of these  $[\text{Fe II}]$  lines are all close each other, so that the extinction correction is not essential either (see Section 2). We collected data on these lines in Cas A from the literature and they are summarized in Section 2, where we also present the data on the SNRs Kepler and RCW 103 for comparison. In Section 3, we present results obtained from the analysis of the line ratios by using the Raymond shock code. In Section 4, we discuss the uncertainty in the results and compare our results to previous optical observations. We then discuss the mass-loss history of the Cas A progenitor star and the origin of QSFs. Finally, in Section 5, we conclude and summarize our paper

## 2. DATA

NIR spectroscopic observations of SNRs are scarce. For Cas A, Gerardy & Fesen (2001) obtained NIR spectra (0.95–2.4  $\mu\text{m}$ ) of three bright QSFs near the southwestern rim of the main ejecta shell and detected strong He I 1.083  $\mu\text{m}$  lines together with  $\text{Pa}\gamma$  and many  $[\text{Fe II}]$  lines in all of them. Lee et al. (2017) carried out long-slit spectroscopy across the main ejecta shell of Cas A and identified seven circumstellar knots corresponding to QSFs. They are characterized by strong He I 1.083  $\mu\text{m}$  and  $[\text{Fe II}]$  lines, and the  $\text{Pa}\gamma$  line has been detected in four of them. The QSFs with both He I 1.083  $\mu\text{m}$  and  $\text{Pa}\gamma$  line data are marked in Figure 1 and their line flux

ratios He I 1.083/Pa $\gamma$  are listed in Table 1 together with the flux ratios of Fe II forbidden lines. Note that the [Fe II] lines at 1.534, 1.600, and 1.664  $\mu\text{m}$  have comparable critical densities of a few times  $10^4 \text{ cm}^{-3}$ , and their ratios to the [Fe II] 1.644  $\mu\text{m}$  line can be used as a density tracer (e.g., see Koo et al. 2016). The intensities of the three lines are weak, so we add them to increase the signal-to-noise ratio, i.e.,  $[\text{Fe II}] 1.534+ / [\text{Fe II}] 1.644 \equiv ([\text{Fe II}] 1.534 + [\text{Fe II}] 1.600 + [\text{Fe II}] 1.664) / [\text{Fe II}] 1.644$ . For those QSFs without all three [Fe II] line fluxes, we have derived  $[\text{Fe II}] 1.534+ / [\text{Fe II}] 1.644$  by using the relation among the line ratios in statistical equilibrium at  $T=10,000 \text{ K}$ , which is almost temperature-independent (see Note in Table 1). Note that the line ratios in Table 1 have not been corrected for extinction because the wavelengths of He I 1.083  $\mu\text{m}$  and Pa $\gamma$  (1.094  $\mu\text{m}$ ) are nearly the same and also the wavelengths of the [Fe II] lines are comparable with each other. For  $A_V = 6 \text{ mag}$ , for example,  $[\text{Fe II}] 1.534+ / [\text{Fe II}] 1.644$  would be higher than those in Table 1 by  $\sim 10\%$ . In Table 1, we also list the line ratios observed in the SNRs Kepler and RCW 103 for comparison. As far as we are aware, these two SNRs are the only ones with published He I 1.083  $\mu\text{m}$  and Pa $\gamma$  line fluxes other than Cas A. The data on the Kepler SNR are from Gerardy & Fesen (2001) and they represent the line ratios of a bright circumstellar knot along the northwest rim of the remnant. The data on RCW 103 are from Oliva et al. (1990) and they represent the line ratios of a bright spot of the optical filament that could be either circumstellar or interstellar material.

### 3. ANALYSIS

#### 3.1. He I 1.083 $\mu\text{m}$ Line and Pa $\gamma$ Emissivity of Shocked Gas

The He I 1.083  $\mu\text{m}$  line is emitted from  $\text{He}^0$  with spin  $S = 1$  (i.e., the triplet  $\text{He}^0$ ) in the decay of  $2^3\text{P}$  to  $2^3\text{S}$ . The line is a triplet composed of three components at 1.08321, 1.08332, and 1.08333  $\mu\text{m}$ . At low densities, the line is due to recombination of  $\text{He}^+$  to  $\text{He}^0$ . At high densities, the line strength can be greatly enhanced by collisional excitation from the lower level  $2^3\text{S}$  which is metastable (e.g., Osterbrock & Ferland 2006; Draine 2011). The emissivity of the He I 1.083  $\mu\text{m}$  line for conditions typical of gaseous nebula has been calculated by several authors (Brocklehurst 1972; Kingdon & Ferland 1993; Benjamin et al. 1999; Porter et al. 2012, 2013). We use the Case B emissivity of Porter et al. (2012, 2013). In radiative shocks, the resonance lines of He I (and H I) are scattered many times, so the Case B limit, where all photons from the permit-

ted transitions to the ground states of these ions are assumed to be reabsorbed “on the spot,” is an appropriate assumption (e.g., Raymond 1979). Porter et al. provided a machine-readable table covering electron densities  $10 \text{ cm}^{-3} \leq n_e \leq 10^{14} \text{ cm}^{-3}$  (in 1 dex steps) and temperatures  $5000 \text{ K} \leq T_e \leq 25,000 \text{ K}$  (in 1000 K steps). The emissivity of Porter et al. is shown in Figure 2 as a function of temperature at  $\log n_e = 1, 2, 3, 4, 5$ , and 6. The  $y$ -axis is  $4\pi j_{10830,r} / n_e n(\text{He}^+)$  where  $j_{10830,r}$  is the He I 1.083  $\mu\text{m}$  emissivity due to recombination. At low densities, the emissivity increases with  $n_e$  due to the contribution from the collisional excitation from the  $2^3\text{S}$  level. When the density becomes higher than  $\sim 10^5 \text{ cm}^{-3}$ , however, the population of the  $2^3\text{S}$  level becomes independent of  $n_e$  because the population rate due to recombination is balanced by the depopulation rate due to collisional transition to singlet states and collisional ionization (e.g., Kingdon & Ferland 1993). We compute the emissivities employing cubic spline interpolation in  $\log T_e$  and linear interpolation/extrapolation in  $\log n_e$  for temperatures within the provided range. He I 1.083  $\mu\text{m}$  emission in shocked gas is mostly from the gas in this temperature range. For computational purposes, the emissivities outside the provided temperature range are obtained by linear extrapolation in  $\log T_e$  (dotted line in Figure 2).

In shocked gas, the He I 1.083  $\mu\text{m}$  line can also be emitted due to collisional excitation from the ground state of the singlet  $\text{He}^0 1^1\text{S}$ ; if some He in the preshock gas is partly neutral, there can be a substantial number of neutral He atoms just behind the shock front, where they can be excited to high energy levels by collisions with electrons and can cascade down to lower energy levels. For high-velocity radiative shocks, this collisionally excited emission behind the shock front is usually much weaker than the recombination emission in the cooling layer, but for low-velocity shocks, it can be a major emission mechanism for some He I lines including the 1.083  $\mu\text{m}$  line. We calculate the He I 1.083  $\mu\text{m}$  line emissivity due to collisional excitation from the  $1^1\text{S}$  state following CHIANTI 8 and MAPPINGS, where the effective collision strengths of Bray et al. (2000) and Sawey & Berrington (1993) for  $n \leq 5$ , covering temperatures  $T = 5000\text{--}500,000 \text{ K}$  and  $T = 2000\text{--}30,000 \text{ K}$ , respectively, are smoothly connected in temperature, and the results are provided as a function of normalized temperatures (e.g., Dopita et al. 2013). In Figure 2, we compare the emissivity due to collisional excitation with that from recombination. Note that the former is proportional to  $n_e n(\text{He}^0)$  and we show  $4\pi j_{10830} / n_e n(\text{He}^+)$  with  $n(\text{He}^0) / n(\text{He}^+) = 0.1$ . We can see that a small fraction of neutral He in hot gas just behind the shock

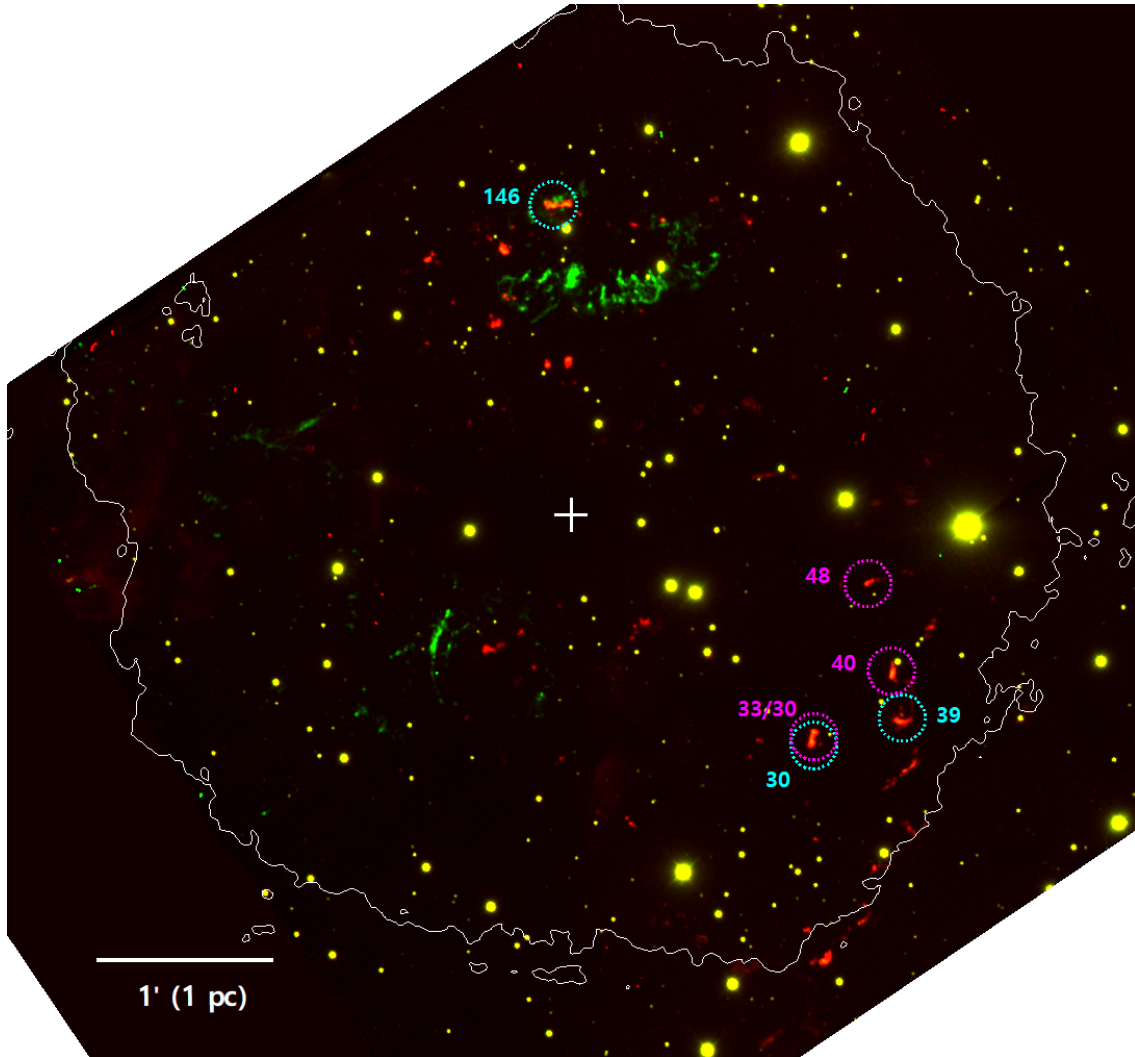


**Figure 1.** A two-color image of Cas A: red =  $H\alpha$ , green =  $H\alpha$  continuum. North is up and east is to the left. The images have been obtained by using the Gemini telescope. QSFs with He I  $1.083\,\mu\text{m}$  line data available are marked in purple (Gerardy & Fesen 2001) and cyan (Lee et al. 2017). The numbers are Knot IDs in Koo et al. (2018). The cross symbol represents the explosion center at  $(\alpha_{2000}, \delta_{2000}) = (23^{\text{h}}23^{\text{m}}27^{\text{s}}.77, +58^{\circ}48'49''.4)$  (Thorstensen et al. 2001), while the thin white contours mark the outer boundary of the SNR in radio corresponding to the intensity level of  $0.3\,\text{mJy beam}^{-1}$  in a Very Large Array 6 cm image (DeLaney et al. 2004).

front can make a significant contribution to the He I  $1.083\,\mu\text{m}$  emission.

Hydrogen  $\text{Pa}\gamma$  emission from a shocked gas is also due to both recombination and collisional excitation from the ground state  $1^2\text{S}$ . For the recombination emissivity, we have fitted the Case B emissivities of Storey & Hummer (1995) who provided a machine-readable table covering  $n_e = 10^2\text{--}10^{10}\,\text{cm}^{-3}$  and temperatures  $T = 500\text{--}30,000\,\text{K}$ . The emissivity depends weakly on  $n_e$  and decreases smoothly with  $T$  (Figure 2). We compute emissivities at  $(n_e, T)$  by employing bilinear interpolation/extrapolation. For the emissivity due to collisional excitation from the ground state, we use the results of Giovanardi et al. (1987) and Anderson et al.

(2000), who provided numerical fits to the effective collision strengths of the transitions between the first 15 levels of  $n$  in the range of temperatures between  $5000\,\text{K}$  and  $\lesssim 5 \times 10^5\,\text{K}$ . At higher temperatures, we adopted the collision strengths at  $T = 5 \times 10^5\,\text{K}$ . Figure 2 compares the emissivities due to recombination and collision, i.e.,  $4\pi j_{\text{Pa}\gamma}/n_e n(\text{H}^+)$  with  $n(\text{H}^0)/n(\text{H}^+) = 0.1$ , and it clearly shows that the emission due to collisional excitation can dominate the  $\text{Pa}\gamma$  emissivity if there is a small fraction of neutral H just behind the shock front where the temperature is high.



**Table 1.** He I 1.083/Pa $\gamma$  and [Fe II] Line Ratios of QSFs in Cassiopeia A.

Name (1)	ID (2)	K2019 ID (3)	$\frac{\text{He I } 1.083}{\text{Pa}\gamma}$ (4)	$\frac{[\text{Fe II}] 1.534}{[\text{Fe II}] 1.644}$ (5)	$\frac{[\text{Fe II}] 1.600}{[\text{Fe II}] 1.644}$ (6)	$\frac{[\text{Fe II}] 1.664}{[\text{Fe II}] 1.644}$ (7)	$\frac{[\text{Fe II}] 1.534+}{[\text{Fe II}] 1.644}$ (8)	References (9)
Cassiopeia A	QSF1	K40	29.0(4.3)	0.314(0.015)	0.236(0.015)	0.139(0.015)	0.689(0.026)	1
	QSF2	K33/K30	42.8(6.4)	0.304(0.040)	0.216(0.040)	...	0.638(0.069)	1
	QSF3	K48	34.0(6.8)	0.298(0.010)	0.240(0.010)	0.127(0.010)	0.665(0.017)	1
Cassiopeia A	(1, 3)	K146	29.2(2.8)	...	0.199(0.004)	0.092(0.003)	0.552(0.009)	2
	(5, 4B)	K30	50.5(1.6)	0.312(0.020)	0.196(0.002)	0.110(0.002)	0.618(0.020)	2
	(7, 4)	K39	37.7(6.0)	0.329(0.023)	0.196(0.005)	0.097(0.003)	0.622(0.024)	2
	(7, 5)	K39	30.4(3.1)	...	0.162(0.005)	0.085(0.004)	0.478(0.012)	2
Kepler	...	...	20.2(3.0)	0.243(0.015)	0.164(0.015)	0.104(0.015)	0.511(0.026)	1
RCW 103	pk1	...	8.0(2.2)	0.120(0.012)	0.072(0.008)	0.031(0.008)	0.223(0.016)	3

NOTE—(1) Object name; (2) knot name in reference; (3) Knot ID in Koo et al. (2018); (4)–(8) observed line intensity ratios; (9) references. [Fe II] 1.534+/[Fe II] 1.644 in column (8) represents  $([\text{Fe II}] 1.534 + [\text{Fe II}] 1.600 + [\text{Fe II}] 1.664) / [\text{Fe II}] 1.644$ . For those QSFs without all three [Fe II] line fluxes, we have derived [Fe II] 1.534+/[Fe II] 1.644 by using the relation among the line ratios in statistical equilibrium at  $T = 10,000$  K, which is almost temperature-independent. The uncertainties in parentheses are  $1\sigma$  errors.

**References**— (1) Gerardy & Fesen (2001); (2) Lee et al. (2017); (3) Oliva et al. (1990)

### 3.2. He Abundance for a Gas of Uniform Temperature

Before analysing the shock emission, we derive the He abundance assuming that the line-emitting gas has a uniform temperature. In a radiative shock, the emitting region has a temperature structure, but the emission of H, He, and [Fe II] comes mainly from a cooling layer at  $T = 5000$ – $10,000$  K (e.g., see Koo et al. 2016), so the result obtained assuming a constant temperature is expected to provide a reasonably accurate He abundance.

In Figure 3, we plot He I 1.083/Pa $\gamma$  versus [Fe II] 1.534+/[Fe II] 1.644 of the sources in Table 1. The two dashed lines represent the relation between the two ratios expected for a fully ionized gas of solar abundance at  $T = 5000$  K and  $10,000$  K, respectively, where the solid dots (from left to right) mark the locations at  $n_e = 10^3, 10^4$ , and  $10^5$  cm $^{-3}$ , respectively. The figure clearly shows that the observed He I 1.083/Pa $\gamma$  ratios of Cas A QSFs are a factor of  $\lesssim 5$  higher than the theoretical ratio, while that of RCW 103 is consistent with the ratio expected for an ionized gas of solar abundance. The figure also shows that the densities of QSFs in Cas A and the Kepler SNR are an order of magnitude larger than that of RCW 103. We have derived electron density and He abundance of the sources for  $T = 5000$  K and  $10,000$  K, and the results are given in Table 2. In the table,  $D_{\text{He}}$  is the He overabundance factor relative to solar defined by  $D_{\text{He}} \equiv X(\text{He})/X_{\odot}(\text{He})$  where  $X(\text{He})$  is abundance ratio of He relative to H by number and  $X_{\odot}(\text{He}) = 9.55 \times 10^{-2}$  (Asplund et al. 2009). According to Table 2, RCW 103 has He abundance close to solar ( $D_{\text{He}} = 0.5$ – $1.5$ ), Kepler is slightly overabundant ( $D_{\text{He}} = 1.0$ – $2.6$ ), and Cas A is a factor of 1.3–6.1 overabundant relative to solar.

### 3.3. Shock Analysis

#### 3.3.1. The Shock Code and Input Parameters

In this section, we derive He abundance from a shock analysis. The shock code that we use is the one developed by Raymond (1979) and Cox & Raymond (1985) with updated atomic parameters (see Koo et al. 2016; Seok et al. 2020). The code assumes a 1D steady flow, using the Rankine-Hugoniot jump conditions to find the postshock gas temperatures. Then it uses the fluid equations to compute the density, temperature, and velocity as the gas cools. The perpendicular component of magnetic field is assumed to be frozen in, and it is compressed with the gas as it cools. Calculations of time-dependent ionization calculations including photoionization are used to compute the cooling rate. Magnetic field strength is fixed to  $0.1$   $\mu\text{G}$ . The magnetic field strength of a QSF is expected to be weak because QSFs have expanded considerably after their ejection (e.g., Chevalier & Kirshner 1978). A stronger magnetic field would lower the density in the recombination zone, but it does not significantly affect the He I 1.083/Pa $\gamma$  ratio. For the chemical composition, we adopt the solar abundances of Grevesse & Sauval (1998) modified by the CNO cycle (see below). In the interior of massive stars, H is converted to He by the CNO cycle. If the He abundance relative to H is  $X(\text{He}) = D_{\text{He}}X(\text{He})_{\odot}$  with  $D_{\text{He}}$  as a free parameter, it means that H is depleted by a factor of  $(1 + 4X(\text{He})_{\odot})/(1 + 4X(\text{He})) \approx 1.4/(1 + 0.4D_{\text{He}})$ , e.g., if  $D_{\text{He}} = 2$ , 22% of H is converted to He and  $N(\text{H})/N_{\odot}(\text{H}) = 0.78$ . The abundances of other elements relative to H are enhanced by the same factor (i.e.,  $N_{\odot}(\text{H})/N(\text{H})$ ). Meanwhile, the N abundance is enhanced and the abundances of C and O are reduced

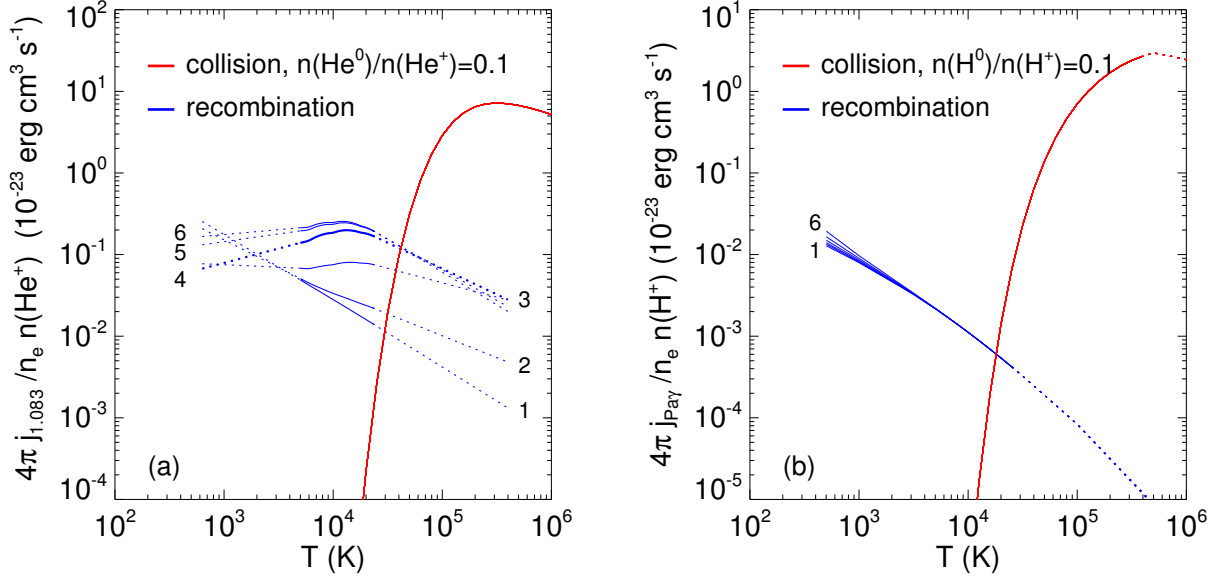


**Figure 2.** (a) He I 1.083  $\mu\text{m}$  emissivity vs. temperature. The emissivities due to recombination and collisional excitation from the  $1^1\text{S}$  level are shown as blue and red, respectively. For the latter, it is assumed that  $n(\text{He}^0)/n(\text{He}^+) = 0.1$ . The recombination emissivities are labeled by  $\log(n_e/\text{cm}^{-3})$ . (b) Same as (a) but for Pa $\gamma$  emissivity.

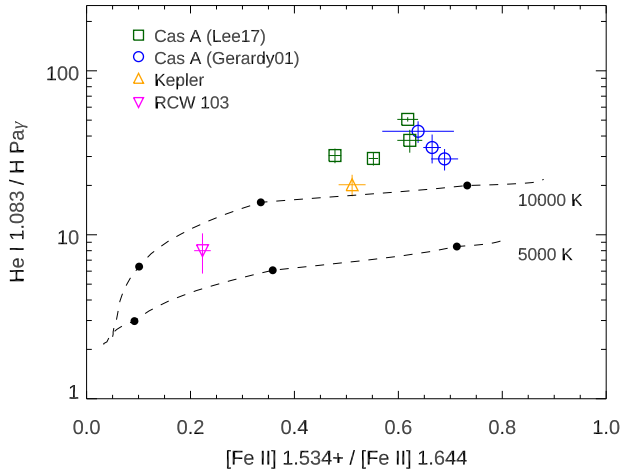


**Figure 3.** He I 1.083  $\mu\text{m}$ /Pa $\gamma$  vs.  $[\text{Fe II}] 1.534+ / [\text{Fe II}] 1.644$  where  $[\text{Fe II}] 1.534+$  represents the sum of  $[\text{Fe II}] 1.534$ ,  $1.600$ , and  $1.677 \mu\text{m}$  line fluxes. The dashed line represents theoretical ratios for fully ionized gas with  $n(\text{He}^+)/n(\text{H}^+) = 0.1$  at  $T = 5000$  K and  $10,000$  K. The black filled circles on each line mark the locations when electron density  $n_e = 10^3 \text{ cm}^{-3}$ ,  $10^4 \text{ cm}^{-3}$ , and  $10^5 \text{ cm}^{-3}$  (from left to right).

by the CNO cycle. We assume that the abundances of C, N, and O are tied to the He abundance and that their relation is given by the internal structure of a  $17 M_\odot$  model star (see Figure 5 in Section 4.3). In this model, when  $D_{\text{He}} = 2$  for example, N abundance is enhanced

by a factor of  $X(\text{N})/X_\odot(\text{N}) = 12$ , and C and O abundances are reduced by factors of 22 and 1.5, respectively. It should be noted that the relation depends on stellar mass and the mixing parameters of the model, although the derived He abundance does not strongly depend on the CNO abundance. It would also be worthwhile to point out that the He abundance of Grevesse & Sauval (1998) adopted for the stellar model calculation is slightly (12%) less than that of Asplund et al. (2009).

An important parameter in shock emission modeling is the ionization levels of H and He in preshock gas entering the shock. They affect the postshock structure and therefore the emission line fluxes (Raymond 1979; Shull & McKee 1979; Cox & Raymond 1985; Hartigan et al. 1987; Dopita & Sutherland 2017; Sutherland & Dopita 2017). They also directly affect the fluxes of collisionally excited Pa $\gamma$  and He I 1.083  $\mu\text{m}$  lines emitted from just behind the shock front, which could be non-negligible for low-velocity shocks (see the Appendix A). In this work, we assume a steady state where the flux of incoming particles being ionized is equal to the flux of ionizing UV radiation emerging from the shock front. For the steady state, the ionization time scale should be shorter than the lifetime or the shock crossing time of QSFs. Considering only H, the ionization time scale is  $t_{\text{ion,H}} = (\Psi_{\text{H}} n_0 v_s \sigma_{\text{H}})^{-1}$  where  $\Psi_{\text{H}}$  is the number of H ionizing photons per H nucleus and  $\sigma_{\text{H}}$  is the photoionization cross section averaged over the radiation field.

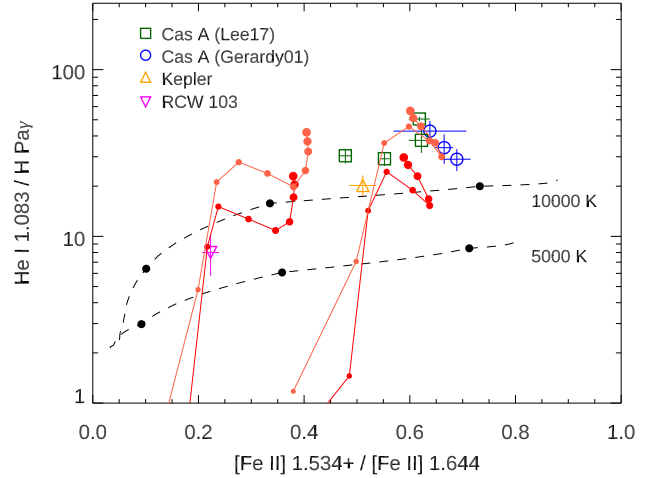
**Table 2.** Electron density and He abundance for a uniform temperature

Object	Knot ID	$T = 5000$ K		$T = 10,000$ K	
		$n_e$	$D(\text{He})$	$n_e$	$D(\text{He})$
(1)	(2)	( $10^4 \text{ cm}^{-3}$ )	(4)	( $10^4 \text{ cm}^{-3}$ )	(6)
Cassiopeia A	QSF1	8.2(2.3, -2.0)	3.3(0.5)	7.5(1.5, -1.4)	1.3(0.2)
	QSF2	5.2(4.4, -2.0)	5.1(0.8)	5.4(3.4, -1.9)	2.0(0.3)
	QSF3	6.3(1.4, -0.7)	4.0(0.8)	6.2(0.9, -0.5)	1.5(0.3)
Cassiopeia A	(1, 3)	3.0(0.2, -0.2)	3.6(0.3)	3.3(0.1, -0.1)	1.4(0.1)
	(5, 4B)	4.5(0.8, -0.6)	6.1(0.2)	4.8(0.6, -0.6)	2.3(0.1)
	(7, 4)	4.7(0.9, -0.8)	4.5(0.7)	4.9(0.7, -0.7)	1.7(0.3)
	(7, 5)	2.0(0.1, -0.1)	4.0(0.4)	2.2(0.1, -0.1)	1.5(0.2)
Kepler	...	2.3(0.3, -0.3)	2.6(0.4)	2.6(0.4, -0.3)	1.0(0.2)
RCW 103	pk1	0.4(0.1, -0.1)	1.5(0.4)	0.5(0.1, -0.1)	0.5(0.2)

NOTE—(1) Object name; (2) Knot ID; (3), (4)  $n_e$  and  $D_{\text{He}}$  at  $T = 5000$  K; (5), (6)  $n_e$  and  $D_{\text{He}}$  at  $T = 10,000$  K. The uncertainties in parentheses are  $1\sigma$  errors.

Using  $\sigma_{\text{H}} \approx 3 \times 10^{-18} \text{ cm}^2$ ,  $t_{\text{ion,H}} \approx 11 \text{ yr } (\Psi_{\text{H}} n_2 v_2)^{-1}$  where  $n_2 = n_0/10^2 \text{ cm}^{-3}$  and  $v_2 = v_s/10^2 \text{ km s}^{-1}$ . For He, the photoionization cross section averaged over the range between the ionization edge at 24.6 eV and the He II at 40.8 eV is  $\sigma_{\text{He}} \approx 4 \times 10^{-18} \text{ cm}^2$  (Reilman & Manson 1979), so the ionization timescale is  $t_{\text{ion,He}} = (\Psi_{\text{He}} n_0 v_s \sigma_{\text{He}})^{-1} \approx (\Psi_{\text{He}} n_2 v_2)^{-1}$  where  $\Psi_{\text{He}}$  is the number of He photoionizing photons per H atom. For a shock speed of  $150 \text{ km s}^{-1}$ ,  $t_{\text{ion,He}} \approx 13 \text{ yr}$ . For comparison, the shock crossing time of the QSF is  $t_{\text{cross}} \approx R/v_s \approx 1 \times 10^2 \text{ yr} \times (R_{-2}/v_2)$  where  $R_{-2} = R/0.01 \text{ pc}$  is the radius of the QSF. The radii of QSFs range from 0.004 pc to 0.06 pc with a mean of 0.01 pc (Koo et al. 2018). The QSFs in Table 1 are bright and large, so their lifetimes might be longer than a few hundred years. They indeed appear in old optical plates to indicate a lifetime  $\gtrsim 60 \text{ yr}$  (Koo et al. 2018). Hence, the steady state between the photoionization flux and neutral particle flux seems to be a reasonable initial condition. The calculation has been done in two steps: we first run the code to obtain  $\Psi$ , which is then used to calculate the ionization fraction of H and He in preshock gas. If  $\Psi < 1$ , the ionization fraction of H is set to be  $\Psi$ , while if  $\Psi \geq 1$ , the incoming H is fully ionized. We therefore adopt  $f(\text{H}^+) = \min(\Psi, 1)$ . The same strategy has been adopted for He and  $\text{He}^+$ . For the input parameters in this work, it has been found that H is fully ionized and He is in the form of  $\text{He}^+$  for shocks with  $v_s \geq 110 \text{ km s}^{-1}$ . The critical velocity is consistent with the results from Shull & McKee (1979) but less than the  $140 \text{ km s}^{-1}$  of Sutherland & Dopita (2017).

The intensities of He I  $1.083 \mu\text{m}$  and  $\text{Pa}\gamma$  lines are obtained in two steps: we first calculate the physical

**Figure 4.** Same as Figure 3 but with shock grids superposed. The left and right grids mark the ratios for preshock densities  $n_0 = 10^2 \text{ cm}^{-3}$  and  $10^3 \text{ cm}^{-3}$ , while the bottom and top grids are for He abundance  $D_{\text{He}} = 1.0$  (bottom) and  $D_{\text{He}} = 2.0$  (top). The red filled circles in each grid mark shock speeds (from left to right)  $v_s = 60 \text{ km s}^{-1}$  to  $240 \text{ km s}^{-1}$  in  $20 \text{ km s}^{-1}$  intervals.

structure of the shocked gas, e.g., temperature and density profiles, H and He ionization fractions, by using the code, and then we derive  $\text{Pa}\gamma$  and He I  $1.083 \mu\text{m}$  line intensities by applying the emissivities in Section 3.1 to the physical structure. We have adopted this procedure because the code does not predict  $\text{Pa}\gamma$ , and because we want to use the more recent calculations of Porter et al. (2012, 2013) for the He I line. This approach is acceptable because these two lines affect the shock structure little. We do not calculate the structure of the radiative

precursor region and the emission from there. The surface brightness of H recombination lines in the precursor region is expected to be very faint, more than an order of magnitude fainter than the brightness of the radiative shock (e.g., [Dopita & Sutherland 2017](#)), so they are not likely to be observed (see also [Koo et al. 2020](#)).

### 3.3.2. Results of Shock Analysis

We have run models with shock speed  $v_s = 60\text{--}240\text{ km s}^{-1}$  in  $20\text{ km s}^{-1}$  steps for a given preshock density and a given He abundance. The red solid lines in Figure 4 show the results obtained for  $n_0 = 10^2\text{ cm}^{-3}$ ,  $10^3\text{ cm}^{-3}$  and  $D_{\text{He}} = 1.0, 2.0$ . The He I  $1.083\text{ }\mu\text{m}/\text{Pa}\gamma$  ratio is proportional to  $D_{\text{He}}$ , and we can see that the ratio is  $\lesssim 1$  at  $v_s \lesssim 80\text{ km s}^{-1}$  and increases abruptly to  $\sim 10$  at  $v_s \gtrsim 100\text{ km s}^{-1}$ . This is because, at low shock velocities, the incoming He atoms are neutral and they remain neutral in the postshock region, so that He I  $1.083\text{ }\mu\text{m}$  flux from recombining He atoms is very small. But as the shock velocity increases, the ionization fraction of He increases and the He I  $1.083\text{ }\mu\text{m}$  flux increases rapidly, more rapidly than the  $\text{Pa}\gamma$  flux, so the He I  $1.083\text{ }\mu\text{m}/\text{Pa}\gamma$  ratio rises steeply. Between  $v_s = 100\text{ km s}^{-1}$  and  $200\text{ km s}^{-1}$ , both He I  $1.083\text{ }\mu\text{m}$  and  $\text{Pa}\gamma$  fluxes increase as  $\propto v_s^3$ , so that their ratio remains roughly a constant ( $\sim 10$ ). And at  $v_s \gtrsim 200\text{ km s}^{-1}$ , He in the incoming gas is mostly  $\text{He}^{2+}$  and the He I  $1.083\text{ }\mu\text{m}$  flux increases more steeply than the  $\text{Pa}\gamma$  flux, so the He I  $1.083\text{ }\mu\text{m}/\text{Pa}\gamma$  ratio increases slowly with  $v_s$  (see the Appendix A for a detailed explanation).

Figure 4 shows that the observed He I  $1.083\text{ }\mu\text{m}/\text{Pa}\gamma$  ratios of QSFs in Cas A clearly require high  $D_{\text{He}} (\sim 2)$ . The [Fe II] line ratio, however, has a degeneracy in  $n_0$  and  $v_s$ , i.e., the same [Fe II] line ratio can be obtained from a shock of low density and high velocity or vice versa. We therefore derive  $n_0$  and  $D_{\text{He}}$  for a range of  $v_s$ . In doing this, we first derive  $n_0$  from the [Fe II]  $1.534\text{ }\mu\text{m}/1.644\text{ }\mu\text{m}$  ratio assuming  $D_{\text{He}} = 1.0$ , and use it to obtain  $D_{\text{He}}$  from He I  $1.083\text{ }\mu\text{m}/\text{Pa}\gamma$ . We then refine  $n_0$  and  $D_{\text{He}}$  by iteration. The exploration has been done on a grid of  $\log n_0$  and  $D_{\text{He}}$  in the ranges  $1.0 \leq \log(n_0/\text{cm}^{-3}) \leq 4.8$  in steps of 0.2 dex steps and  $1.0 \leq D_{\text{He}} \leq 2.8$  in steps of 0.2. It is worthwhile to note that [Fe II]  $1.534\text{ }\mu\text{m}/1.644\text{ }\mu\text{m}$  of some knots is larger than the maximum value, which could be either due to an error in observed ratios or uncertainty in the model parameters. In such cases, we adopt  $n_0 = 10^4\text{ cm}^{-3}$ .

Table 3 shows  $n_0$  and  $D_{\text{He}}$  obtained for shock speeds  $v_s = 80\text{--}240\text{ km s}^{-1}$ . This is a range of shock speeds expected for the majority of QSFs (see Section 4.2). According to Table 3,  $D_{\text{He}}$  of the QSFs in Cas A is mostly

in the range 1.0–3.0 depending on the shock speed.  $D_{\text{He}}$  is smallest at  $v_s = 120\text{ km s}^{-1}$  and is a factor of  $\lesssim 2$  larger at 80 and  $160\text{ km s}^{-1}$ . At higher shock velocities, it becomes smaller (see the Appendix A).

## 4. DISCUSSION

### 4.1. Uncertainties in Shock Analysis

A practical way to infer the uncertainty in  $D_{\text{He}}$  derived from our shock analysis is to examine the result on the SNRs with He abundance close to solar. In the following, we discuss our results on two such SNRs, RCW 103 and Kepler. RCW 103 is a young ( $\sim 2000\text{ yr}$ ; [Carter et al. 1997](#)) SNR interacting with dense ambient medium. The NIR data in Table 1 had been obtained by [Oliva et al. \(1990\)](#) toward a peak position in the bright optical filament in the southern area where the remnant is interacting with a molecular cloud (see [Paron et al. 2006](#), and references therein). [Oliva et al. \(1999\)](#) analyzed Infrared Space Observatory (ISO) infrared spectroscopic data together with their NIR data for the position and concluded that the observed line intensities are compatible with emission from the postshock region behind a fast ( $\gtrsim 300\text{ km s}^{-1}$ ) shock, with a negligible contribution from the radiative precursor. They measured the gas abundances of refractory (Si, Fe, Ni) and nonrefractory (Ne, P, S, Cl, Ar) species and found that all the derived abundances are close to solar. For comparison, we obtained  $n_0 = 20\text{--}80\text{ cm}^{-3}$  and  $D_{\text{He}} \leq 1.1$  for shock speeds between 120 and  $240\text{ km s}^{-1}$  (Table 3). If we adopt the half-width at zero intensity of the [Fe II]  $1.257\text{ }\mu\text{m}$  line ( $230\text{ km s}^{-1}$  after deconvolution of the instrumental resolution) of [Oliva et al. \(1999\)](#) as the shock velocity, we obtain  $n_0 \approx 25\text{ cm}^{-3}$  and  $D_{\text{He}} < 1.0$ . (The observed He I  $1.083\text{ }\mu\text{m}/\text{Pa}\gamma$  ratio is less than the ratio at  $D_{\text{He}} = 1.0$  in the shock model,  $8.0 \pm 2.2$  versus 14.0). The derived  $D_{\text{He}}$  is close to the normal abundance in the interstellar medium (ISM). The preshock density, on the other hand, is smaller than that ( $n_0 \lesssim 300\text{ cm}^{-3}$ ) obtained by [Oliva et al. \(1999\)](#) from the average surface brightness of Br $\alpha$  in the ISO slit ( $14'' \times 20''$ ). A possible explanation might be that there are multiple shock fronts tangential to the line of sight in the ISO slit. Kepler is the remnant of historical supernova SN 1604. Strong Fe K-shell emission and the lack of O emission suggest that it is a remnant of a Type Ia SN ([Reynolds et al. 2007](#); [Yamaguchi et al. 2014](#)). The remnant, however, is interacting with dense, N-enriched CSM likely ejected in a very late phase of the progenitor ([Vink 2017](#)). The NIR data for Kepler in Table 1 were obtained by [Gerardy & Fesen \(2001\)](#) toward a bright circumstellar knot along the northwest rim where the optical emission is the brightest. The optical emission



**Table 3.** He abundance from a shock model analysis

Object	Knot Name	$v_s = 80 \text{ km s}^{-1}$		$v_s = 120 \text{ km s}^{-1}$		$v_s = 160 \text{ km s}^{-1}$		$v_s = 200 \text{ km s}^{-1}$		$v_s = 240 \text{ km s}^{-1}$	
		$n_0$ ( $10^3 \text{ cm}^{-3}$ )	$D_{\text{He}}$ ( $10^3 \text{ cm}^{-3}$ )	$n_0$ ( $10^3 \text{ cm}^{-3}$ )	$D_{\text{He}}$ ( $10^3 \text{ cm}^{-3}$ )	$n_0$ ( $10^3 \text{ cm}^{-3}$ )	$D_{\text{He}}$ ( $10^3 \text{ cm}^{-3}$ )	$n_0$ ( $10^3 \text{ cm}^{-3}$ )	$D_{\text{He}}$ ( $10^3 \text{ cm}^{-3}$ )	$n_0$ ( $10^3 \text{ cm}^{-3}$ )	$D_{\text{He}}$ ( $10^3 \text{ cm}^{-3}$ )
Cassiopeia A	QSF1	$10^a$	3.17 (-0.24, 0.27)	4.18 (-1.36, 4.66)	1.21 ( $\dots$ , 0.17)	1.98 (-0.75, 1.60)	2.06 (-0.31, 0.31)	5.68 (-2.52, $\dots$ )	1.24 (-0.17, 0.17)	5.77 (-2.28, $\dots$ )	$< 1^b$
	QSF2	$10^a$	4.00 (-0.40, 0.36)	1.60 (-0.76, 2.91)	1.95 (-0.29, 0.31)	0.66 (-0.32, 1.12)	3.62 (-0.60, 0.60)	1.68 (-1.10, 7.18)	1.96 (-0.30, 0.31)	2.25 (-1.47, 6.88)	1.50 (-0.23, 0.24)
	QSF3	$10^a$	3.48 (-0.40, 0.40)	2.60 (-0.49, 0.79)	1.48 (-0.29, 0.28)	1.12 (-0.25, 0.28)	2.60 (-0.53, 0.57)	3.16 (-0.96, 1.54)	1.49 (-0.28, 0.29)	3.80 (-1.02, 1.57)	1.15 ( $\dots$ , 0.24)
Cassiopeia A	(1, 3)	1.47 (-0.13, 0.17)	3.60 (-0.19, 0.23)	0.84 (-0.06, 0.05)	1.49 (-0.14, 0.14)	0.35 (-0.03, 0.02)	2.72 (-0.27, 0.27)	0.49 (-0.05, 0.06)	1.53 (-0.14, 0.14)	0.67 (-0.07, 0.09)	1.11 ( $\dots$ , 0.11)
	(5, 4B)	2.96 (-0.71, 1.04)	4.78 (-0.08, 0.07)	1.18 (-0.23, 0.21)	2.43 (-0.08, 0.08)	0.49 (-0.10, 0.09)	4.59 (-0.16, 0.16)	1.17 (-0.32, 0.50)	2.43 (-0.08, 0.08)	1.50 (-0.41, 0.59)	1.84 (-0.06, 0.06)
	(7, 4)	3.77 (-1.20, 3.05)	3.92 (-0.40, 0.39)	1.45 (-0.32, 0.40)	1.74 (-0.27, 0.28)	0.60 (-0.13, 0.16)	3.21 (-0.55, 0.56)	1.30 (-0.41, 0.72)	1.76 (-0.28, 0.29)	1.77 (-0.55, 0.89)	1.33 (-0.22, 0.22)
	(7, 5)	0.67 (-0.07, 0.08)	4.09 (-0.31, 0.28)	0.46 (-0.04, 0.03)	1.73 (-0.17, 0.17)	0.19 (-0.02, 0.01)	3.32 (-0.38, 0.37)	0.22 (-0.02, 0.03)	1.83 (-0.18, 0.19)	0.27 (-0.03, 0.04)	1.30 (-0.14, 0.14)
Kepler	$\dots$	0.93 (-0.21, 0.33)	3.04 (-0.23, 0.25)	0.68 (-0.12, 0.15)	1.01 ( $\dots$ , 0.23)	0.29 (-0.05, 0.06)	1.94 (-0.29, 0.30)	0.30 (-0.05, 0.06)	1.17 ( $\dots$ , 0.16)	0.39 (-0.10, 0.15)	$< 1^b$
RCW 103	pk1	0.08 (-0.01, 0.01)	2.44 (-0.24, 0.27)	0.08 (-0.01, 0.01)	$< 1^b$	0.04 (-0.00, 0.01)	1.33 ( $\dots$ , 0.36)	0.03 (-0.00, 0.00)	$< 1^b$	0.02 (-0.00, 0.00)	$< 1^b$

NOTE—The uncertainties in parentheses are  $1\sigma$  errors. The uncertainties marked with “ $\dots$ ” indicate that either  $n_0 \pm \sigma$  or  $D_{\text{He}} \pm \sigma$  is outside the range of parameter values of the shock model.

<sup>a</sup> Preschock density is fixed to  $10^4 \text{ cm}^{-3}$  because the observed  $[\text{Fe II}]1.534 + [\text{Fe II}]1.644$  ratio is larger than the maximum ratio predicted by the shock model for given  $v_s$ .

<sup>b</sup> The observed He I 1.083/Pa $\gamma$  ratio is less than that at  $D_{\text{He}} = 1$  predicted by the shock model for given  $v_s$ .

of this area has been analyzed by several authors (Dennefeld 1982; Leibowitz & Danziger 1983; Blair et al. 1991; Dopita et al. 2019). Dopita et al. (2019) carried out a detailed shock analysis of the optical spectra of the knots slightly to south of the knot analyzed in this work by using the MAPPINGS code. They found that metals are not depleted, perhaps except C, and that He abundance is solar. The shock speed and the preshock density that they obtained were  $220 \text{ km s}^{-1}$  and  $600 \text{ cm}^{-3}$ , respectively. For comparison, we obtained  $n_0 = 290\text{--}680 \text{ cm}^{-3}$  and  $D_{\text{He}} = 1.0\text{--}1.9$  for shock speeds  $120\text{--}240 \text{ km s}^{-1}$ . If we use the shock speed of Dopita et al. (2019), we obtain  $n_0 = 330 \text{ cm}^{-3}$  and  $D_{\text{He}} \leq 1.0$ . (The observed He I  $1.083 \mu\text{m}/\text{Pa}\gamma$  ratio is less than the ratio at  $D_{\text{He}} = 1.0$  in the shock model,  $20.2 \pm 3.0$  versus  $22.2$ .) The derived  $D_{\text{He}}$  agrees well with the normal ISM abundance. Note that the N overabundance of the CSM in Kepler is a factor of  $\lesssim 2$  (Dopita et al. 2019; Kasuga et al. 2021), and it could be partly due to the radial N abundance gradient of the Galaxy. So the He abundance is expected to be close to solar. On the other hand, our  $n_0$  is factor of  $\sim 2$  lower than that of Dopita et al. (2019). Considering that the two observations are independent observations, the discrepancy in  $n_0$  is acceptable.

In summary, the He abundances derived for RCW 103 and Kepler are all close to solar. This result is consistent with the expected result for these SNRs, and it supports  $D_{\text{He}}$  from our shock code analysis. The shock velocities in these SNRs are high and the preshock H and He are fully ionized, so that the uncertainty in  $D_{\text{He}}$  due to the preshock ionization fraction can be neglected. For low shock speeds ( $< 100 \text{ km s}^{-1}$ ), however,  $D_{\text{He}}$  from the shock model strongly depends on preshock ionization fraction. For example, for a  $60 \text{ km s}^{-1}$  shock with  $n_0 = 100 \text{ cm}^{-3}$ , the He I  $1.083/\text{Pa}\gamma$  ratio varies by an order of magnitude depending on the preshock ionization state of H and He, e.g.,  $0.23$  in a “self-consistent” model where H and He are almost neutral versus  $3.8\text{--}4.7$  in H (and He) ionized models (see Appendix A). Since the self-consistent model requires a steady state where the ionization time scale is being shorter than the shock crossing time, the self-consistent model may not be applicable to small QSFs (see Section 3.3.1). Also, the preshock gas can be ionized by radiation fields from the SNR reverse and forward shocks (e.g., see Raymond et al. 2018; Laming & Temim 2020). In that case,  $D_{\text{He}}$  in Table 3 for the  $v_s = 80 \text{ km s}^{-1}$  case could be considered as an upper limit. As far as the QSFs in Table 3 are concerned, they are all bright and large QSFs, so that the steady state condition is likely achieved.

On the other hand, radiative shocks are known to be subject to thermal instabilities, which can make the

shock velocity oscillate around its steady-state value and the postshock flow turbulent (Chevalier & Imamura 1982; Innes et al. 1987; Sutherland et al. 2003). According to these theoretical studies, shocks faster than  $120\text{--}150 \text{ km s}^{-1}$  are unstable, and the emission line ratios of unstable, nonsteady shocks could be significantly different from those of steady shocks. In our study, we assumed a plane-parallel and steady shock, and derived He abundance and preshock density for given shock velocities. If thermal instabilities operate in shocks propagating into QSFs, the steady shock models in Table 3 might not be applicable. However, while these instabilities cause large variations in the emission line ratios on small scales, observational studies indicate that the average spectra and derived abundances are not strongly affected (Dopita et al. 2019; Raymond et al. 2020). Hence, we consider that our conclusion that  $D_{\text{He}} \lesssim 3$  in most of QSFs is robust.

#### 4.2. Comparison with Previous Optical Observations

Chevalier & Kirshner (1978) analyzed the optical spectra of two bright QSFs in the northern main shell of Cas A obtained by Kirshner & Chevalier (1977) and, from the observed He I  $\lambda 5876/\text{H}\beta$  ratios, concluded that He is overabundant relative to H by a factor of 10 or 4 depending on the correction for interstellar extinction (i.e.,  $A_V = 4.3$  or  $6.5$ ). The overabundance factor of 10 is much larger than  $D_{\text{He}} (\lesssim 3)$  of the knots derived in this work. Chevalier & Kirshner (1978) used for comparison the  $50\text{--}60 \text{ km s}^{-1}$  shock models of Raymond (1979) because the observed line intensities of [O III]  $\lambda 5007$  and H recombination lines implied a shock speed lower than  $80 \text{ km s}^{-1}$ . The two QSFs that they observed correspond to K146 in Figure 1. We note that  $N(\text{H})$  toward K146 is  $(1.2\text{--}1.33) \times 10^{22} \text{ cm}^{-2}$  according to the map of H column density of Hwang & Laming (2012) obtained from X-ray spectral analysis, which corresponds to  $A_V = 6.4\text{--}7.0$  using  $A_V/N_{\text{H}} = 1.87 \times 10^{21} \text{ cm}^{-2} \text{ mag}^{-1}$ . Hence, the larger extinction ( $6.5$ ) is possible, in which case the overabundance factor would be 4.

On the other hand, the shock speed ( $50\text{--}60 \text{ km s}^{-1}$ ) of Chevalier & Kirshner (1978) is relatively low. The velocities of QSFs obtained from their proper motions and radial velocities are  $\lesssim 400 \text{ km s}^{-1}$  (Kamper, & van den Bergh 1976; van den Bergh & Kamper 1985; Alarie et al. 2014). These velocities represent the *apparent* motions of QSFs, which are due to both shock motion and systematic expansion. The systematic expansion velocity of QSFs acquired during the ejection from the progenitor star is uncertain (see Kamper, & van den Bergh (1976); van den Bergh & Kamper (1985)), and the shock velocities might vary from QSF to QSF depend-

ing on their densities and environments. The pressure behind the Cas A SNR shock front has been estimated as  $\sim 2 \times 10^7 \text{ cm}^{-3} (\text{km s}^{-1})^2$  (Koo et al. 2018). If QSFs are located behind the SNR shock front, therefore, the velocity of the shock propagating into a QSF would be  $v_s \simeq 140(n_0/10^3 \text{ cm}^{-3})^{1/2} \text{ km s}^{-1}$  where  $n_0$  is the density of the QSF. For one QSF, Koo et al. (2020) obtained a high-resolution spectrum of the [Fe II] 1.257  $\mu\text{m}$  line, and its velocity width is  $\sim 150 \text{ km s}^{-1}$ . So the typical shock velocity is expected to be  $\gtrsim 100 \text{ km s}^{-1}$ . If the shock speed of K146 is indeed 50–60  $\text{km s}^{-1}$ , either its density is high or it could be located in a relatively low-pressure region. Alternatively the [O III]  $\lambda 5007$  flux of the QSF in Chevalier & Kirshner (1978) could have been underestimated. The QSF K146 is superposed on the main SN ejecta shell with strong [O III]  $\lambda 5007$  emission, so it seems to be difficult to obtain an accurate flux of the faint QSF emission.

#### 4.3. Mass-loss History of the Cas A Progenitor and the Origin of QSFs

The chemical abundance of QSFs is an indicator of the evolutionary stage of the progenitor star at the time of the QSF ejection. Lamb (1978) pointed out that, based on the observed high abundance of N, QSFs were ejected from the N-rich layer at the bottom of the H envelope of a 9–25  $M_\odot$  model star at the end of core H burning, although the He abundance of that layer in their model stars was considerably lower than the value observed by Chevalier & Kirshner (1978), i.e.,  $D_{\text{He}} \simeq 10$  for  $A_V = 4.3$ . As an example, we show in Figure 5 the internal structure of a 17  $M_\odot$  star of solar metallicity at the end of the core H-burning stage obtained by using the MESA code (Paxton et al. 2011, 2013, 2015). According to the model, the star has an outer H envelope of original abundance at  $M_r \gtrsim 10 M_\odot$  and an inner H envelope with H partially converted to He by the CNO cycle between  $M_r \simeq 10 M_\odot$  and  $6 M_\odot$  where  $M_r$  is the mass inside a radius  $r$  from the center. In the inner H envelope, the mass fraction of  $^4\text{He}$  increases from 0.28 to 0.66 while that of H decreases from 0.70 to 0.32, so that  $D_{\text{He}}$  varies from 1.0 to 5.2. Meanwhile, the  $^{14}\text{N}$  abundance increases from  $1.01 \times 10^{-3}$  to  $1.17 \times 10^{-2}$  as C and O are converted to  $^{14}\text{N}$  by the CNO cycle. The corresponding N overabundance factor relative to H,  $D_{\text{N}} (\equiv X(\text{N})/X_\odot(\text{N})) = 1$  to 25. The N overabundance factor of QSFs relative to H is a factor of 7–10 (Chevalier & Kirshner 1978; Alarie et al. 2014). The He overabundance factor of QSFs derived in this study is mostly in the range of  $D_{\text{He}} = 1.0$ –3.3 (Table 3). So both the N and He mass abundances of QSFs match to those of the inner H envelope layer, and, as has already been

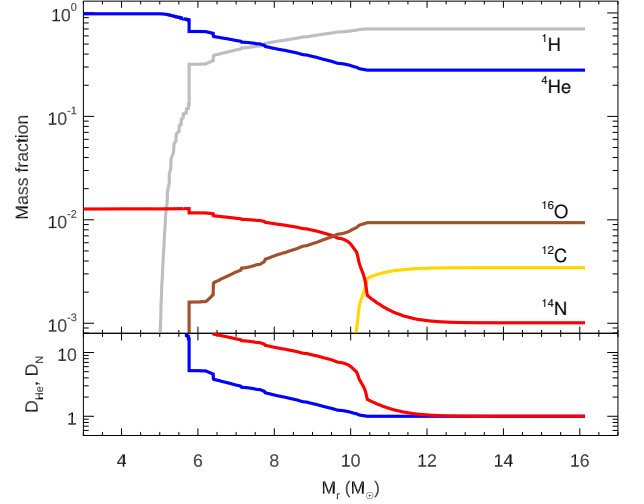


**Figure 5.** Top: internal chemical composition of a 17  $M_\odot$  star of solar metallicity at the end of the core H-burning stage obtained by using the MESA code. Bottom: profiles of the He and N overabundance factors (see text). We have adopted the Ledoux criterion for convection with a semiconvection efficiency of  $\alpha_{\text{SEMI}} = 1.0$  and a step overshoot scheme using a step function over a layer of thickness  $l_{\text{OV}} = 0.3H_P$  above the hydrogen-burning convective core. For stellar wind mass-loss rates, we have used the Dutch scheme in MESA with the Dutch scaling factor of 1.0. The star loses 0.86  $M_\odot$  by hot winds during the main sequence. The abscissa is the mass inside a radius  $r$  from the center.

pointed out by Chevalier & Kirshner (1978) and Lamb (1978), this suggests that the Cas A progenitor had lost a substantial amount of the H envelope at the time of the QSF ejection, e.g.,  $\gtrsim 60\%$  of the H envelope in the model star in Figure 5. The inner chemical structure, however, depends on the initial mass of the star and the adopted physical assumptions on the convection criterion, overshooting, semiconvection, mass loss and rotation. Therefore, our discussion based on the model prediction should only be considered as indicative.

Here we do not adjust the physical parameters to obtain a model consistent with the observation, but simply adopt the default values of the MESA code except for the overshooting and semiconvection parameters:  $l_{\text{ov}} = 0.3H_P$  where  $H_P$  is the local pressure scale height at the outer boundary of the H-burning convective core, and  $\alpha_{\text{SEMI}} = 1.0$  (see also the caption of Figure 5). These values are comparable to those adopted by Brott et al. (2011) who calibrated stellar evolution models using a large sample of the observed OB-type main-sequence stars in the Small and Large Magellanic Clouds and in the Milky Way.

Cas A is an SN of Type IIb (Krause et al. 2008), and the progenitor of a Type IIb SN is most likely in a binary

system that has its hydrogen envelope removed mainly by Roche-lobe overflow rather than by stellar wind mass loss (Joss et al. 1988; Podsiadlowski et al. 1993; Stancliffe & Eldridge 2009; Claeys et al. 2011; Yoon et al. 2017, and references therein). The most likely binary interaction is Case B mass transfer, meaning that the mass transfer from the primary star starts during He core contraction. This is because the stellar radius expands most significantly during this phase (e.g., Podsiadlowski et al. 1993). The mass of the Cas A progenitor star has been estimated to be 15–25  $M_{\odot}$  (Young et al. 2006; see also Koo & Park 2017 and the references therein), so the progenitor would rapidly expand and have a steady wind shortly after the end of the main sequence when the helium core contracts. As the envelope of the primary star expands and fills the Roche lobe the binary mass transfer (Case B) would start. The surface He mass fraction of the progenitor at this stage is likely  $Y_s = 0.28$  (Figure 5). Chemical mixing induced by rotationally induced hydrodynamic instabilities might lead to a significant He enhancement at the surface by the end of main sequence (e.g., Heger et al. 2000; Maeder & Meynet 2000). However, as discussed by Yoon et al. (2010), the primary star on the main sequence in a Case B binary system would be a slow rotator because of tidal synchronization, and the impact of rotation on the primary star would not be significant. The mass transfer rate could be as high as  $\dot{M} \sim 10^{-2} M_{\odot} \text{ yr}^{-1}$  for the case of stable mass transfer (e.g., Yoon et al. 2010). The secondary star would be spun-up to the critical rotation when it accretes matter from the primary star because the transferred matter carries angular momentum. The secondary star would therefore undergo strong mass-loss enhancement due to rotation (e.g., Yoon et al. 2010; Langer 2012). This means that a large amount of the matter transferred to the secondary might be ejected as a wind from the secondary star. Most of the ejected mass at this stage has solar abundance ( $Y_s = 0.28$ ), but the material ejected from the innermost layer of the H envelope has higher  $Y_s$ . The total amount of the transferred mass and the subsequent evolution of the progenitor depend sensitively on the binary parameters (e.g., see Stancliffe & Eldridge 2009; Yoon et al. 2017). If the initial period  $P$  of the binary system is sufficiently long (i.e.,  $P \gtrsim 1000$  days), the primary star could remain as an RSG throughout its evolution until the SN explosion. Otherwise, after the Case B mass transfer, the primary star would go through a blue-loop phase before it explodes as an SN (e.g., Stancliffe & Eldridge 2009; Yoon et al. 2017). Therefore, QSFs could be the dense clumps within the wind ejected from the secondary star as a result of nonconservative stable Case

B mass transfer or within the wind ejected from the primary star after the binary mass transfer. A caveat is that Cas A has likely undergone the common envelope evolution resulting from unstable mass transfer. Cas A shows no evidence for a companion star (Kerzendorf et al. 2019, and references therein), so the companion star could possibly have been a low-mass main-sequence star that has merged with the giant envelope of the primary star (e.g., see Lohev et al. 2019). In the common envelope system, the progenitor can lose the H envelope much more rapidly (i.e., on a dynamical timescale) than in the case of stable mass transfer if common envelope ejection occurs. So, in this case, QSFs could be dense clumps ejected in the common envelope phase.

Although we used the term “clumps in the wind” or “clumps ejected” for QSFs above, it is not clear when and how the clumps became dense ( $\sim 10^3 \text{ cm}^{-3}$ ). An idea, which was proposed in a single-star progenitor scenario, is that QSFs are fragments of dense circumstellar shell crushed by the SN blast wave (Chevalier & Liang 1989; Garcia-Segura et al. 1996). In this scenario, the Cas A SN exploded in a cavity surrounded by a dense shell of RSG wind material compressed by the fast wind in the subsequent blue supergiant or Wolf-Rayet phase of the progenitor star. The shell is disrupted due to hydrodynamic instabilities, and the dense fragments of the shell appear as QSFs when they are swept up by the SN blast wave. Later, Chevalier & Oishi (2003) pointed out that QSFs are not spatially confined to a shell structure, so they proposed that QSFs are dense clumps embedded in a smooth, inhomogeneous RSG wind rather than the fragments of disrupted circumstellar shell. Indeed the spatial distribution of QSFs is highly asymmetric: there is a large population of QSFs in the western area (Koo et al. 2018), and there are also QSFs aligned along a prominent arc in the southern area that had been known from early optical observations (van den Bergh & Kamper 1983, 1985; Lawrence et al. 1995). It is not clear, however, how such asymmetric structures of dense knots could be produced in an RSG wind. There have been suggestions that the Cas A progenitor had a brief blue or yellow supergiant phase with a fast wind immediately prior to the explosion (Hwang & Laming 2009; Koo et al. 2020; Weil et al. 2020), but this is not likely to have affected the overall distribution of QSFs unless QSFs themselves are the dense clumps in the fast wind. In the binary progenitor scenario, the major mass loss probably occurred very rapidly. The structure of circumbinary matter might be asymmetric and complex, possibly with partial shells, arcs, and/or spiral structures depending on binary parameters and wind speed. In this regard, it is worth noting that the reverse shock motion suggests



that the SN blast wave has been interacting with a dense shell; in the western area, the reverse shock moves backward, which could be explained by a partial dense shell in that area or by the SN explosion in an asymmetric massive circumstellar shell (Orlando et al. 2022; Vink et al. 2022). The highly asymmetric distribution of QSFs with organized structures seems to suggest the interaction of the SN blast wave with a clumpy circumbinary medium.

## 5. SUMMARY

We have collected NIR spectroscopic data on several QSFs in Cas A from the literature and analyzed their He I  $1.083\ \mu\text{m}/\text{Pa}\gamma$  ratios together with the ratios of [Fe II] lines by using the Raymond shock code. We have found that the He abundance of QSFs is mostly enhanced by a factor of  $\lesssim 3$  relative to solar. The observed He abundance of QSFs, together with their N abundance, indicates that QSFs originated from the bottom layer of the H envelope of the progenitor star during the post-main-sequence phase. The H envelope is most likely to have been removed by Roche-lobe overflow in the binary system and ejected from the system to create the CSM around the Cas A SN. The highly asymmetric distribution of QSFs with organized structures suggests that the ejection was highly anisotropic, although it is uncertain when and how QSFs achieved their current shapes, i.e., isolated dense clumps. A detailed study of the kinetic properties of QSFs will be helpful to understand the origin of QSFs. In the following, we summarize the main results of this work.

1. We surveyed the available NIR observations of QSFs in Cas A and summarized their He I  $1.083\ \mu\text{m}/\text{Pa}\gamma$  ratios and the ratios of [Fe II] lines (Table 1). These line ratios provide a reliable estimate of electron density and He abundance of shocked gas. We also list in the table the line ra-

tios observed in the SNRs Kepler and RCW 103 for comparison. Kepler is the remnant of historical supernova SN 1604 (Type Ia) and RCW 103 is a young ( $\sim 2000$  yr) SNR interacting with dense ambient medium. All line ratios are from the literature.

2. We have found that the He I  $1.083\ \mu\text{m}/\text{Pa}\gamma$  ratios of Cas A QSFs are higher than that of RCW 103 by a factor of 3.6–6.3 and also higher than that of Kepler by a factor of 1.5–2.5. The observed He I  $1.083\ \mu\text{m}/\text{Pa}\gamma$  ratios of Cas A QSFs are a factor of  $\lesssim 6$  higher than the ratio expected for an ionized gas of solar abundance at  $(0.5\text{--}1.0)\times 10^4$  K.
3. We have analyzed the line ratios by using the Raymond shock code. There is a degeneracy in preshock density  $n_0$  and shock speed  $v_s$ , so we derive the He abundance for a range of  $v_s$  (80–240 km  $\text{s}^{-1}$ ). According to our analysis, the He abundance of QSFs in Cas A is mostly enhanced by a factor of 1.0–3.3 relative to solar. For comparison, the He abundances derived for RCW 103 and Kepler are all close to solar. The He abundances of QSFs, together with their N abundances, indicate that QSFs originated from the bottom layer of the H envelope of the progenitor star during the post-main-sequence phase.

We thank R. Benjamin for helpful discussions about the emissivity of He I I  $1.083\ \mu\text{m}$ . We thank J. Seok for providing the  $\text{H}\alpha$  line and continuum images used in Figure 1. This research was supported by Basic Science Research Program through the National Research Foundation of Korea (NRF) funded by the Ministry of Science, ICT and future Planning (2020R1A2B5B01001994).

*Software:* CHIANTI (Dere et al. 1997; Del Zanna et al. 2015)

## APPENDIX

### A. $\text{Pa}\gamma$ AND He I $1.083\ \mu\text{m}$ LINES FROM RADIATIVE SHOCKS AND THEIR FLUX RATIOS

In this appendix, we describe the emission characteristics of  $\text{Pa}\gamma$  and He I  $1.083\ \mu\text{m}$  lines from radiative shocks. We focus on the dependence of the He I  $1.083\ \mu\text{m}/\text{Pa}\gamma$  ratio on shock speed and preshock ionization fraction of H and He, which are the main parameters determining the physical structure and the emission

characteristics of a radiative shock. We fix the density of ions and neutrals in the ambient medium to  $n_0 = 100\ \text{cm}^{-3}$  and the magnetic field strength  $B_0 = 0.1\ \mu\text{G}$ . The abundance is assumed to be the solar abundances of Asplund et al. (2009) except for N, which is assumed to be enhanced by a factor of 5.

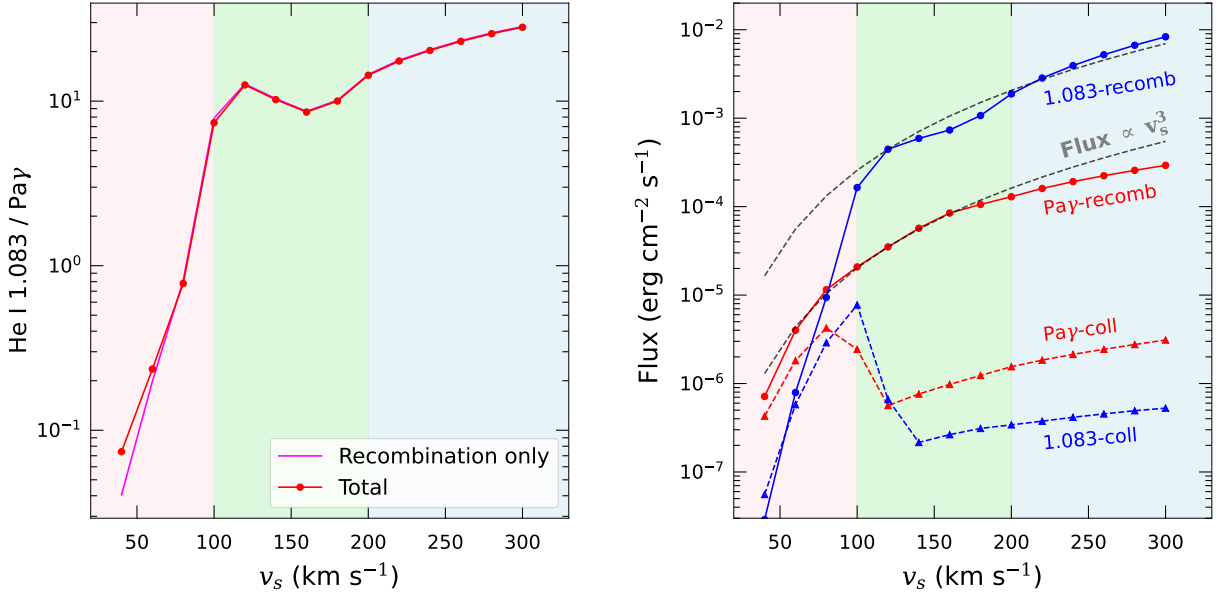


**Figure 6.** Left: shock speed vs. He I 1.083  $\mu\text{m}/\text{Pa } \gamma$ . The red line shows the ratio for total (recombination + collisional) flux, while the magenta line shows the ratio for recombination line flux. The filled circles are plotted on the line at intervals of 20 km s $^{-1}$ . Right: shock speed vs. Pa  $\gamma$  and He I 1.083  $\mu\text{m}$  line fluxes. The solid and dotted lines denote recombination and collisionally excited line fluxes, respectively. The gray dashed lines show the relation “Flux  $\propto v_s^3$ ”. The different colors in the background indicate the range of shock speeds with different behaviors of the line ratio (see text).

#### A.1. Dependence of He I 1.083 $\mu\text{m}/\text{Pa } \gamma$ Ratio on Shock Speed

Figure 6(left) shows the He I 1.083  $\mu\text{m}/\text{Pa } \gamma$  ratio as a function of shock speed, and is identical to Figure 4 except that the  $x$ -axis is shock speed. We can see that the line ratio increases steeply with velocity at  $v_s \lesssim 100$  km s $^{-1}$ , remains constant at around 10 between  $v_s \simeq 100$  km s $^{-1}$  and 200 km s $^{-1}$ , and gradually increases with shock speed at  $v_s > 200$  km s $^{-1}$ . Such velocity dependence of the line ratio is basically due to the variation of He I 1.083  $\mu\text{m}$  flux with shock speed. This is shown in Figure 6(right) where, for both Pa  $\gamma$  and He I 1.083  $\mu\text{m}$  lines, the line fluxes from collisional excitations and recombinations are plotted separately. Before discussing the He I 1.083  $\mu\text{m}$  line, we first examine the properties of the Pa  $\gamma$  line, which can be summarized as follows (see also Cox 1972; Raymond 1979; Hollenbach & McKee 1989). (1) The flux of the collisionally excited line is substantial at  $v_s \lesssim 80$  km s $^{-1}$ . At higher shock velocities, the recombination line flux dominates. (2) The recombination line flux increases with shock velocity monotonically. It is well fitted by  $F_{\text{Pa}\gamma} \propto v_s^3$  between  $v_s = 60$  km s $^{-1}$  and 160 km s $^{-1}$ . This implies that a roughly constant fraction of shock energy is converted to the hydrogen recombination line radiation. At lower velocities, it rises steeply due to the rapid increase in the ionization fraction of the incoming hydrogen gas. At higher velocities, the preshock hydrogen is fully ionized

and the velocity dependence flattens, i.e.,  $F_{\text{Pa}\gamma} \propto v_s^{2.0}$ . Raymond (1979) obtained the same velocity dependence for H $\beta$  at low shock velocities (50–200 km s $^{-1}$ ) where we obtained  $F_{\text{Pa}\gamma} \propto v_s^{3.0}$ . But, because the incoming hydrogen atoms were assumed to be fully ionized in his models (models A-I), the two results are consistent. On the other hand, Dopita & Sutherland (1996) obtained a steeper relation,  $F_{\text{H}\beta} \propto v_s^{2.41}$  in the velocity range 150–500 km s $^{-1}$ . They did not present the values of preshock ionization fraction, but the hydrogen in the incoming gas might be fully ionized because the critical velocity for hydrogen to be fully ionized is 150 km s $^{-1}$  in their models. The larger slope could be due to the difference in atomic parameters and/or numerical treatments determining the shock structure.

The variation of He I 1.083  $\mu\text{m}$  line flux with shock speed is similar to the variation of the Pa  $\gamma$  line flux but with some differences. First, at  $v_s < 100$  km s $^{-1}$ , the recombination line flux rises much more steeply than compared to the Pa  $\gamma$  recombination line flux. Second, between  $v_s \simeq 100$  km s $^{-1}$  and 200 km s $^{-1}$ , the recombination line flux roughly follows  $F_{1.083} \propto v_s^3$ , but there is a kink at  $v_s \simeq 160$  km s $^{-1}$ . Finally, at  $v_s \geq 180$  km s $^{-1}$ , the recombination line flux increases with shock speed monotonically, with a larger spectral index than the Pa  $\gamma$  flux,  $F_{1.083} \propto v_s^{3.9}$ . Note that these differences are manifested in the velocity dependence of the line ratio in Figure 6(left), i.e.,  $F_{1.083}/F_{\text{Pa}\gamma} \propto v_s^{1.9}$ . Below,

we explain why the He I 1.083  $\mu\text{m}$  line flux shows such behavior with shock speed.

(i)  $v_s < 100 \text{ km s}^{-1}$  (see Fig. 7(a)): Incoming H and He are mostly neutral, so that the collisionally excited line emission is substantial at the shock front. Because of the rapid cooling, H and He in shocked gas cannot reach collisional ionization equilibrium, and the neutral fraction is kept high throughout the postshock region. In particular,  $\text{He}^0$ , which has a relatively high ionization potential, stays almost neutral. Since there are few  $\text{He}^+$  ions to recombine, the He I 1.083  $\mu\text{m}$  recombination line flux is suppressed to a low level. As the shock velocity increases, the fraction of  $\text{He}^+$  in the recombination plateau region at  $T_e \sim 10^4 \text{ K}$  increases, and the He I 1.083  $\mu\text{m}$  recombination line flux rises steeply. When the shock velocity reaches  $\sim 100 \text{ km s}^{-1}$ ,  $\text{He}^0$  in the recombination plateau is almost fully ionized to  $\text{He}^+$ , so that the shocks faster than  $100 \text{ km s}^{-1}$  show different characteristics.

(ii)  $100 \text{ km s}^{-1} \leq v_s \leq 200 \text{ km s}^{-1}$  (see Fig. 7(b)). Incoming H and He are mostly singly ionized, so that there is little emission from collisionally excited lines at the shock front. Thermal energy of the shocked gas is removed gradually, so that the temperature remains roughly constant up to  $N_H \sim 1 \times 10^{17} \text{ cm}^{-2}$ . Meanwhile  $\text{He}^+$  is ionized to  $\text{He}^{2+}$ . Then the temperature drops abruptly to  $\sim 7000 \text{ K}$  due to the high cooling rate resulting from high electron density and the presence of ionized He and ionized metals. Most of the He I 1.083  $\mu\text{m}$  flux originates from this cooling region where the  $\text{He}^+$  fraction is high. As the velocity increases, the  $\text{He}^+$  fraction in the incoming gas decreases owing to the increase in the  $\text{He}^+$  ionizing photons ( $h\nu > 54.6 \text{ eV}$ ). Consequently, the  $\text{He}^{2+}$  fraction in the postshock region increases. Recall from Figure 6 that the He I 1.083  $\mu\text{m}$  recombination line flux and therefore the He I 1.083  $\mu\text{m}/\text{Pa}\gamma$  ratio fluctuate in this velocity range with a minimum at  $v_s \sim 160 \text{ km s}^{-1}$ . This is because the  $\text{He}^+$  fraction in the recombination plateau decreases with velocity for  $v_s = 120\text{--}160 \text{ km s}^{-1}$  but increases with velocity for  $v_s = 160\text{--}200 \text{ km s}^{-1}$ . It increases at high velocities because the ionizing UV photon flux for  $\text{He}^0$  from shocked gas increases (Cox 1972; Raymond 1979; Binette et al. 1985).

(iii)  $v_s > 200 \text{ km s}^{-1}$  (see Fig. 7(c)). The temperature structure is almost identical to the previous case,

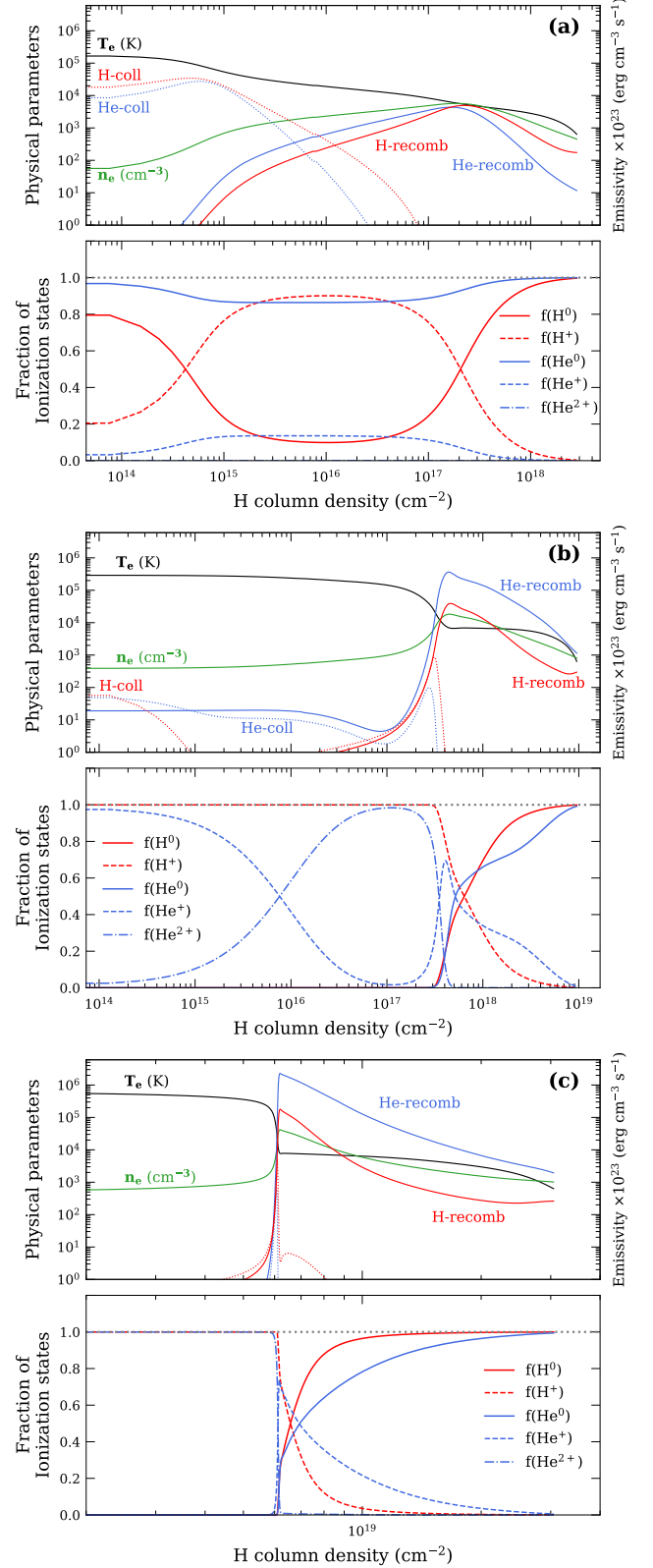


**Figure 7.** Structure of shocks propagating into an ambient medium of  $n_0 = 10^2 \text{ cm}^{-3}$  at (a)  $80 \text{ km s}^{-1}$ , (b)  $140 \text{ km s}^{-1}$ , and (c)  $220 \text{ km s}^{-1}$ . The emissivity profiles of  $\text{Pa}\gamma$  and He I 1.083  $\mu\text{m}$  lines due to collisional excitation and recombination are shown together with  $T_e$ ,  $n_e$ , and the ionization structure of H and He.

**Table 4.** He I 1.083  $\mu\text{m}$  and Pa $\gamma$  Line Fluxes of a 60 km s $^{-1}$  Shock for Different Preshock Ionization Fractions

Model	$f_0$			$2\pi$ Line Flux				$\frac{\text{He I 1.083}}{\text{Pa}\gamma}$
	$\text{H}^0$	$\text{He}^0$	$\text{He}^+$	$(10^{-6} \text{ erg cm}^{-2} \text{ s}^{-1})$				
				$\text{Pa}\gamma\text{-coll.}$	$\text{Pa}\gamma\text{-recomb.}$	1.083-coll.	1.083-recomb.	
Self-consistent	0.974	0.998	0.001	1.82	3.99	0.577	0.785	0.23
H ionized	0.001	0.998	0.001	0.185	10.1	22.5	19.9	3.81
H, He ionized	0.001	0.001	0.999	0.239	10.3	0.334	48.8	4.67

NOTE— $f_0$  denotes preshock ionization fraction. The *coll.* and *recomb.* in the line flux column denote collisionally excited and recombination line flux, respectively.

showing a plateau and an abrupt temperature drop. However, in contrast to the intermediate-speed shocks, essentially all He is doubly ionized at the shock front, so He in the postshock region remains mostly He $^{2+}$  until the temperature drops to  $T_e \sim 10^5$  K, at which point a significant amount of He $^+$  is produced via recombination. Shocks faster than 200 km s $^{-1}$  show almost the same structure. The dependence of He recombination line flux on shock speed is steeper than that of the Pa $\gamma$  line, i.e.,  $F_{1.083} \propto v_s^{3.9}$ , because the collisional excitation from the metastable state depends strongly on shock speed.

In summary, the dependence of the He I 1.083  $\mu\text{m}$  recombination line flux on shock velocity, which is responsible for the variation in line ratio, is closely related to the H and He ionization structure of the shock. At  $v_s < 100$  km s $^{-1}$ , the ionization fractions of H and He in the incoming gas increase rapidly with shock velocity, so the flux and the He I 1.083  $\mu\text{m}$ /Pa $\gamma$  ratio rise steeply. Between  $v_s = 100$  km s $^{-1}$  and 200 km s $^{-1}$ , H and He in the incoming gas are mostly singly ionized, and Pa $\gamma$  and He I 1.083  $\mu\text{m}$  both increase  $\propto v_s^3$ , so that their ratio remains roughly a constant ( $\sim 10$ ). At  $v_s > 200$  km s $^{-1}$ , He in the incoming gas is mostly He $^{2+}$  and  $F_{1.083} \propto v_s^{3.9}$ , while  $F_{\text{Pa}\gamma} \propto v_s^{2.0}$ , so that  $F_{1.083}/F_{\text{Pa}\gamma} \propto v_s^{1.9}$ .

#### A.2. Dependence of He I 1.083 $\mu\text{m}$ /Pa $\gamma$ Ratio on Preshock Ionization Fraction

The ionization fractions of H and He in preshock gas entering the shock are important parameters in shock emission modeling, especially for the calculation of H and He line intensities (see Raymond 1979; Shull & McKee 1979; Cox & Raymond 1985; Dopita & Sutherland 2017; Sutherland & Dopita 2017). In this work, we assumed a steady state where the flux of incoming particles being ionized is equal to the flux of ionizing UV

radiation emerging from the shock front (Section 3.3.1). In this “self-consistent” model, the preshock ionization fraction is determined from the shock structure, and, in slow ( $v_s \lesssim 100$  km s $^{-1}$ ) shocks, H and He in preshock gas remain predominantly neutral because the ionizing radiation from postshock gas was insufficient. However, in some environments, the preshock gas could be exposed to other sources of photoionizing radiation in the surrounding area. In such cases, the ionization fractions of H and He could be higher than those of the self-consistent models, and the recombination line flux could be enhanced (see below). For example, in Cas A, the X-ray and EUV emissions from the SNR reverse and forward shocks could increase the ionization fractions of unshocked material in the SNR (e.g., see Raymond et al. 2018; Laming & Temim 2020). Here we examine how the high ionization fractions of H and He in preshock gas affect He I 1.083  $\mu\text{m}$  and Pa $\gamma$  fluxes and their ratios.

We consider a 60 km s $^{-1}$  shock propagating into an ambient medium with  $n_0 = 100 \text{ cm}^{-3}$  and  $B_0 = 0.1 \mu\text{G}$ . In the self-consistent model, the majority of H and He in preshock gas is mostly neutral, i.e.,  $[f_0(\text{H}^0), f_0(\text{He}^0), f_0(\text{He}^+)] = [0.974, 0.998, 0.001]$ . In this case, the He I 1.083  $\mu\text{m}$  fluxes from collision-excited and recombination lines are comparable, whereas for the Pa $\gamma$  line, the recombination line flux is two times the collision-excited line flux, so that  $F_{1.083}/F_{\text{Pa}\gamma} = 0.23$ . In order to see the effect of high H and He ionization fractions, we simply consider the cases where either the preshock H is fully ionized or (H, He) are both singly ionized, i.e.,  $[f_0(\text{H}^0), f_0(\text{He}^0), f_0(\text{He}^+)] = [0.001, 0.998, 0.001]$  and  $[0.001, 0.001, 0.999]$ . Table 4 shows the line fluxes and their ratios in three models. We see that when the preshock H is ionized,  $F_{1.083}/F_{\text{Pa}\gamma}$  becomes higher than that in the self-consistent model by more than an order of magnitude. When H is ionized but He is not, the collision-excited and recombination He I 1.083  $\mu\text{m}$  fluxes are enhanced by a factors of 39 and 25, respec-



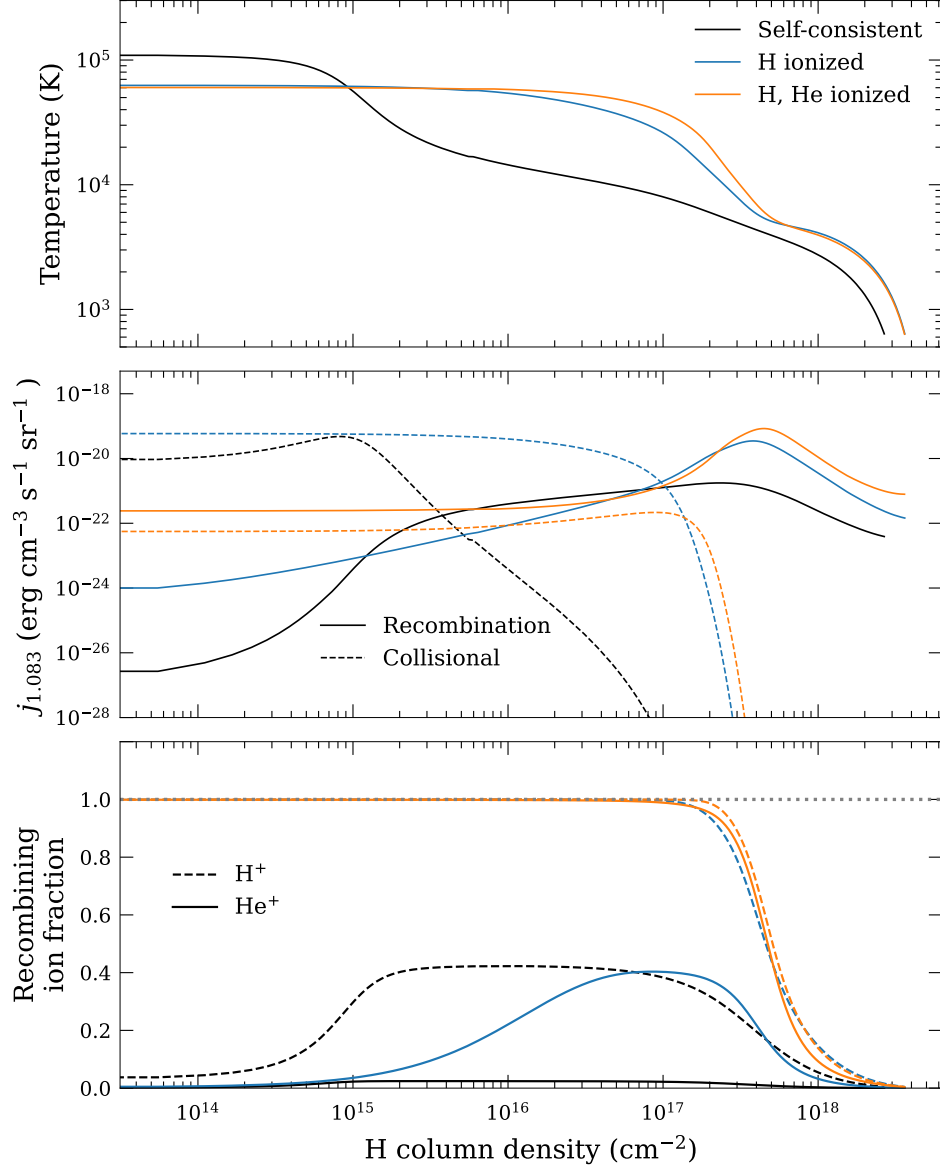


**Figure 8.** Shock structure of models of different preshock ionization fractions (see text). The profiles of temperature, emissivity of the He I 1.083  $\mu\text{m}$  line, and ionization fractions of  $\text{H}^+$  and  $\text{He}^+$  are shown from top to bottom.

tively. This is mainly because, due to the lack of the major coolant  $\text{H}^0$ , the shocked gas stays hot ( $\sim 6 \times 10^4$  K) for a long time compared to the self-consistent model (see Figure 8). The upper state of He I 1.083  $\mu\text{m}$  ( $2^3\text{P}$ ) is 21.0 eV above the ground state ( $1^1\text{S}$ ), so the collisional excitation is efficient in hot shocked gas. On the other hand, since there is enough time, a substantial fraction ( $\lesssim 40\%$ ) of He is ionized to  $\text{He}^+$ , so the recombination He I 1.083  $\mu\text{m}$  line flux is also enhanced. The  $\text{Pa}\gamma$  recombination line flux also increases but by much less than the increase in the He I 1.083  $\mu\text{m}$  recombination line flux. Therefore,  $F_{1.083}/F_{\text{Pa}\gamma}$  is increased by a factor of  $\sim 17$ . In the case where both H and He are ion-

ized, the shock profiles are not much different from the model where only H is ionized (Figure 8). But, because the ionization state of He is kept as  $\text{He}^+$  in the cooling layer, the He I 1.083  $\mu\text{m}$  recombination line flux, which is proportional to  $\text{He}^+$  fraction, is even higher than in the model where H is ionized but He is not. On the other hand, the collision-excited He I 1.083  $\mu\text{m}$  line flux decreases because the fraction of  $\text{He}^0$  is low. But it decreases only slightly because the shocked gas remains hot for a little longer. The  $\text{Pa}\gamma$  flux is almost the same. Hence,  $F_{1.083}/F_{\text{Pa}\gamma}$  becomes 4.67, which is a factor of  $\sim 20$  larger than in the self-consistent model.

The above example shows that, for slow shocks, the He I  $1.083\,\mu\text{m}/\text{Pa}\gamma$  ratio depends strongly on the ionization fraction of H and He in preshock gas: the ratio is higher when the H and He ionization fractions are higher. Hence, considering that the He I  $1.083\,\mu\text{m}/\text{Pa}\gamma$  ratio is almost linearly proportional to the He abundance,  $D_{\text{He}}$  derived from the model can vary by more than a order of magnitude depending on the H and He ionization fractions. However, at least we can conclude from the above shock models that if preshock H or He

is ionized,  $D_{\text{He}}$  will be much smaller than the values we derived in Section 3.3 using slow self-consistent shock models. Hence,  $D_{\text{He}}$  for an  $80\,\text{km s}^{-1}$  shock in Table 3 may be considered as an upper limit. For fast shocks ( $v_s > 100\,\text{km s}^{-1}$ ), H is fully ionized and He is mostly  $\text{He}^+$  and  $\text{He}^{2+}$ , so even if ionization fraction was overestimated or underestimated, the line flux ratio is little affected because the gas at the shock front is rapidly ionized due to the high temperature in the postshock region.

## REFERENCES

- Alarie, A., Bilodeau, A., & Drissen, L. 2014, MNRAS, 441, 2996
- Aldering, G., Humphreys, R. M., & Richmond, M. 1994, AJ, 107, 662
- Anderson, H., Ballance, C. P., Badnell, N. R., & Summers, H. P. 2000, J. Phys. B: At. Mol. Opt. Phys. 33 1255
- Asplund, M., Grevesse, N., Sauval, A. J., & Scott, P. 2009, ARA&A, 47, 481
- Aver, E., Olive, K. A., & Skillman, E. D. 2015, JCAP, 2015, 011. doi:10.1088/1475-7516/2015/07/011
- Benjamin, R. A., Skillman, E. D., & Smits, D. P. 1999, ApJ, 514, 307
- Binette, L., Dopita, M. A., & Tuohy, I. R. 1985, ApJ, 297, 476. doi:10.1086/163544
- Blair, W. P., Long, K. S., & Vancura, O. 1991, ApJ, 366, 484. doi:10.1086/169583
- Bray, I., Burgess, A., Fursa, D. V., et al. 2000, A&AS, 146, 481. doi:10.1051/aas:2000277
- Brocklehurst, M. 1972, MNRAS, 157, 211
- Brott, I., de Mink, S. E., Cantiello, M., et al. 2011, A&A, 530, A115. doi:10.1051/0004-6361/201016113
- Carter, L. M., Dickel, J. R., & Bomans, D. J. 1997, PASP, 109, 990. doi:10.1086/133971
- Chevalier, R. A. & Imamura, J. N. 1982, ApJ, 261, 543. doi:10.1086/160364
- Chevalier, R. A., & Kirshner, R. P. 1978, ApJ, 219, 931
- Chevalier, R. A. & Liang, E. P. 1989, ApJ, 344, 332. doi:10.1086/167802
- Chevalier, R. A., & Oishi, J. 2003, ApJ, 593, L23
- Claeys, J.S.W., de Mink, S.E., Pols, O.R., Eldridge, J.J., Baes, M. 2011, A&A, 528, A131
- Clegg, R. E. S. 1987, MNRAS, 229, 31P. doi:10.1093/mnras/229.1.31P
- Clegg, R. E. S., & Harrington, J. P. 1989, MNRAS, 239, 869
- Cox, D. P. 1972, ApJ, 178, 143. doi:10.1086/151774
- Cox, D. P. & Raymond, J. C. 1985, ApJ, 298, 651. doi:10.1086/163649
- Davies, B. & Dessart, L. 2019, MNRAS, 483, 887. doi:10.1093/mnras/sty3138
- Del Zanna, G., Dere, K. P., Young, P. R., et al. 2015, A&A, 582, A56. doi:10.1051/0004-6361/201526827
- DeLaney, T., Rudnick, L., Fesen, R. A., et al. 2004, ApJ, 613, 343
- Dennefeld, M. 1982, A&A, 112, 215
- Dere, K. P., Landi, E., Mason, H. E., et al. 1997, A&AS, 125, 149. doi:10.1051/aas:1997368
- Dinerstein, H. 1995, The Analysis of Emission Lines: A Meeting in Honor of the 73th Birthdays of D. E. Osterbrock & M. J. Seaton (Cambridge: Cambridge Univ. Press), 134
- Dopita, M. A. & Sutherland, R. S. 2017, ApJS, 229, 35. doi:10.3847/1538-4365/aa6542
- Dopita, M. A., Seitzzahl, I. R., Sutherland, R. S., et al. 2019, AJ, 157, 50. doi:10.3847/1538-3881/aaf235
- Dopita, M. A. & Sutherland, R. S. 1996, ApJS, 102, 161. doi:10.1086/192255
- Dopita, M. A., Sutherland, R. S., Nicholls, D. C., et al. 2013, ApJS, 208, 10. doi:10.1088/0067-0049/208/1/1020
- Draine, B. T. 2011, Physics of the Interstellar and Intergalactic Medium (Princeton, NJ: Princeton Univ. Press)
- Fesen, R. A., Becker, R. H., & Blair, W. P. 1987, ApJ, 313, 378. doi:10.1086/164974 The Fate of the Most Massive Stars, ed. R. M. Humphreys & K. Z. Stanek, 323
- Garcia-Segura, G., Langer, N., & Mac Low, M.-M. 1996, A&A, 316, 133
- Gerardy, C. L. & Fesen, R. A. 2001, AJ, 121, 2781
- Giovanardi, C., Natta, A., & Palla, F. 1987, A&AS, 70, 269
- Grevesse, N. & Sauval, A. J. 1998, SSRv, 85, 161. doi:10.1023/A:1005161325181
- Hartigan, P., Raymond, J., & Hartmann, L. 1987, ApJ, 316, 323. doi:10.1086/165204
- Heger, A., Langer, N., & Woosley, S.E. 2000, ApJ, 528, 368
- Hollenbach, D., & McKee, C. F. 1989, ApJ, 342, 306
- Hwang, U., & Laming, J. M. 2009, ApJ, 703, 883

- Hwang, U., & Laming, J. M. 2012, *ApJ*, 746, 130
- Innes, D. E., Giddings, J. R., & Falle, S. A. E. G. 1987, *MNRAS*, 226, 67. doi:10.1093/mnras/226.1.67
- Izotov, Y. I., Thuan, T. X., & Guseva, N. G. 2014, *MNRAS*, 445, 778. doi:10.1093/mnras/stu1771
- Joss, P.C., Podsiadlowski, Ph., Hsu, J.J.L., & Rappaport, S. 1988, *Nature*, 331, 237
- Kamper, K., & van den Bergh, S. 1976, *ApJS*, 32, 351
- Kasuga, T., Vink, J., Katsuda, S., et al. 2021, *ApJ*, 915, 42. doi:10.3847/1538-4357/abff4f
- Kerzendorf, W. E., Do, T., de Mink, S. E., et al. 2019, *A&A*, 623, A34. doi:10.1051/0004-6361/201732206
- Kingdon, J., & Ferland, G. J. 1993, *ApJ*, 403, 211
- Kirshner, R. P. & Chevalier, R. A. 1977, *ApJ*, 218, 142. doi:10.1086/155666
- Koo, B.-C., Kim, H.-J., Lee, Y.-H., et al. 2018, *ApJ*, 866, 139
- Koo, B.-C., Kim, H.-J., Oh, H., et al. 2020, *Nature Astronomy*, 4, 584. doi:10.1038/s41550-019-0996-4
- Koo, B. C., & Park, C. 2017, in *Handbook of Supernovae*, ed. A. Alsabti & P. Murdin (Cham: Springer), 161
- Koo, B.-C., Raymond, J. C., & Kim, H.-J. 2016, *Journal of Korean Astronomical Society*, 49, 109
- Krause, O., Birkmann, S. M., Usuda, T., et al. 2008, *Science*, 320, 1195
- Lamb, S. A. 1978, *ApJ*, 220, 186
- Laming, J. M. & Hwang, U. 2003, *ApJ*, 597, 347. doi:10.1086/378268
- Laming, J. M. & Temim, T. 2020, *ApJ*, 904, 115. doi:10.3847/1538-4357/abc1e5
- Langer, N. 2012, *ARA&A*, 50, 107
- Lawrence, S. S., MacAlpine, G. M., Uomoto, A., et al. 1995, *AJ*, 109, 2635
- Lee, J.-J., Park, S., Hughes, J. P., & Slane, P. O. 2014, *ApJ*, 789, 7
- Lee, Y.-H., Koo, B.-C., Moon, D.-S., Burton, M. G., & Lee, J.-J. 2017, *ApJ*, 837, 118
- Lee, Y.-H., Koo, B.-C., Moon, D.-S., & Lee, J.-J. 2015, *ApJ*, 808, 98
- Leibowitz, E. M. & Danziger, I. J. 1983, *MNRAS*, 204, 273. doi:10.1093/mnras/204.2.273
- Lohev, N., Sabach, E., Gilkis, A., et al. 2019, *MNRAS*, 490, 9. doi:10.1093/mnras/stz2593
- Maeder, A., & Meynet, G. 2000, *ARA&A*, 38, 143
- McKee, C. F., Chernoff, D. F., & Hollenbach, D. J. 1984, *Infrared Spectroscopy of Interstellar Shocks, in Galactic and Extragalactic Infrared Spectroscopy*, eds. M. F. Kessler, J. P. Phillips (Reidel; Dordrecht), 103
- McKee, C. F., & Cowie, L. L. 1975, *ApJ*, 195, 715
- Minkowski, R. 1968, in *Nebulae and Interstellar Matter*, ed. B. M. Middlehurst & L. H. Aller (Chicago, IL: Univ. Chicago Press), 623
- Nisini, B. 2008, *Jets from Young Stars II, Lecture Notes in Physics*, Vol. 742 (Berlin: Springer), 79
- Oliva, E., Moorwood, A. F. M., & Danziger, I. J. 1989, *A&A*, 214, 307
- Oliva, E., Moorwood, A. F. M., & Danziger, I. J. 1990, *A&A*, 240, 453
- Oliva, E., Moorwood, A. F. M., Drapatz, S., et al. 1999, *A&A*, 343, 943
- Orlando, S., Wongwathanarat, A., Janka, H.-T., et al. 2022, *A&A*, 666, A2. doi:10.1051/0004-6361/202243258
- Osterbrock, D. E., & Ferland, G. J. 2006, *Astrophysics of gaseous nebulae and active galactic nuclei* (University Science Books)
- Paron, S. A., Reynoso, E. M., Purcell, C., et al. 2006, *PASA*, 23, 69. doi:10.1071/AS06003
- Paxton, B., Bildsten, L., Dotter, A., et al. 2011, *ApJS*, 192, 3. doi:10.1088/0067-0049/192/1/3
- Paxton, B., Cantiello, M., Arras, P., et al. 2013, *ApJS*, 208, 4. doi:10.1088/0067-0049/208/1/4
- Paxton, B., Marchant, P., Schwab, J., et al. 2015, *ApJS*, 220, 15. doi:10.1088/0067-0049/220/1/15
- Peimbert, M., & van den Bergh, S. 1971, *ApJ*, 167, 223
- Peimbert, M. & Torres-Peimbert, S. 1987, *RMxAA*, 15, 117
- Podsiadlowski, Ph., Hsu, J.J.L., Joss, P.C., & Ross, R.R., 1993, *Nature*, 364, 509
- Porter, R. L., Ferland, G. J., Storey, P. J., et al. 2012, *MNRAS*, 425, L28
- Porter, R. L., Ferland, G. J., Storey, P. J., et al. 2013, *MNRAS*, 433, L89
- Raymond, J. C. 1979, *ApJS*, 39, 1
- Raymond, J. C., Koo, B.-C., Lee, Y.-H., et al. 2018, *ApJ*, 866, 128. doi:10.3847/1538-4357/aadf93
- Raymond, J. C., Chilingarian, I.V., Blair, W.P., et al., 2020, *ApJ*, 894, 108. doi:10.3847/1538-4357/ab886d
- Reed, J. E., Hester, J. J., Fabian, A. C., & Winkler, P. F. 1995, *ApJ*, 440, 706
- Reilman, R. F. & Manson, S. T. 1979, *ApJS*, 40, 815. doi:10.1086/190605
- Reynolds, S. P., Borkowski, K. J., Hwang, U., et al. 2007, *ApJL*, 668, L135. doi:10.1086/522830
- Sawey, P. M. J. & Berrington, K. A. 1993, *Atomic Data and Nuclear Data Tables*, 55, 81. doi:10.1006/adnd.1993.1017
- Seok, J. Y., Koo, B.-C., Zhao, G., et al. 2020, *ApJ*, 893, 79. doi:10.3847/1538-4357/ab800b
- Shull, J. M. & McKee, C. F. 1979, *ApJ*, 227, 131. doi:10.1086/156712

- Smith, N. 2014, *ARA&A*, 52, 487.  
doi:10.1146/annurev-astro-081913-040025
- Stancliffe, R., & Eldridge, J.J. 2009, *MNRAS*, 396, 1699
- Storey, P. J., & Hummer, D. G. 1995, *MNRAS*, 272, 41
- Sutherland, R. S., Bicknell, G. V., & Dopita, M. A. 2003, *ApJ*, 591, 238. doi:10.1086/375294
- Sutherland, R. S. & Dopita, M. A. 2017, *ApJS*, 229, 34.  
doi:10.3847/1538-4365/aa6541
- Takami, M., Chrysostomou, A., Bailey, J., et al. 2002, *ApJL*, 568, L53
- Takami, M., Usuda, T., Sugai, H., et al. 2002, *ApJ*, 566, 910
- Thorstensen, J. R., Fesen, R. A., & van den Bergh, S. 2001, *AJ*, 122, 297
- van den Bergh, S. 1971, *ApJ*, 165, 457
- van den Bergh, S., & Kamper, K. 1983, *ApJ*, 268, 129
- van den Bergh, S., & Kamper, K. 1985, *ApJ*, 293, 537
- Vink, J. 2017, in *Handbook of Supernovae*, ed. A. Alsabti & P. Murdin (Cham: Springer), 139
- Vink, J., Patnaude, D. J., & Castro, D. 2022, *ApJ*, 929, 57.  
doi:10.3847/1538-4357/ac590f
- Vink, J. S. 2022, *ARA&A*, 60, 203.  
doi:10.1146/annurev-astro-052920-094949
- Weil, K. E., Fesen, R. A., Patnaude, D. J., et al. 2020, *ApJ*, 891, 116. doi:10.3847/1538-4357/ab76bf
- Yamaguchi, H., Badenes, C., Petre, R., et al. 2014, *ApJL*, 785, L27. doi:10.1088/2041-8205/785/2/L27
- Yoon, S.-C., Dessart, L., & Clocchiatti, A. 2017, *ApJ*, 840, 10. doi:10.3847/1538-4357/aa6afe
- Yoon, S.-C., Woosley, S. E., & Langer, N. 2010, *ApJ*, 725, 940
- Young, P. A., Fryer, C. L., Hungerford, A., et al. 2006, *ApJ*, 640, 891